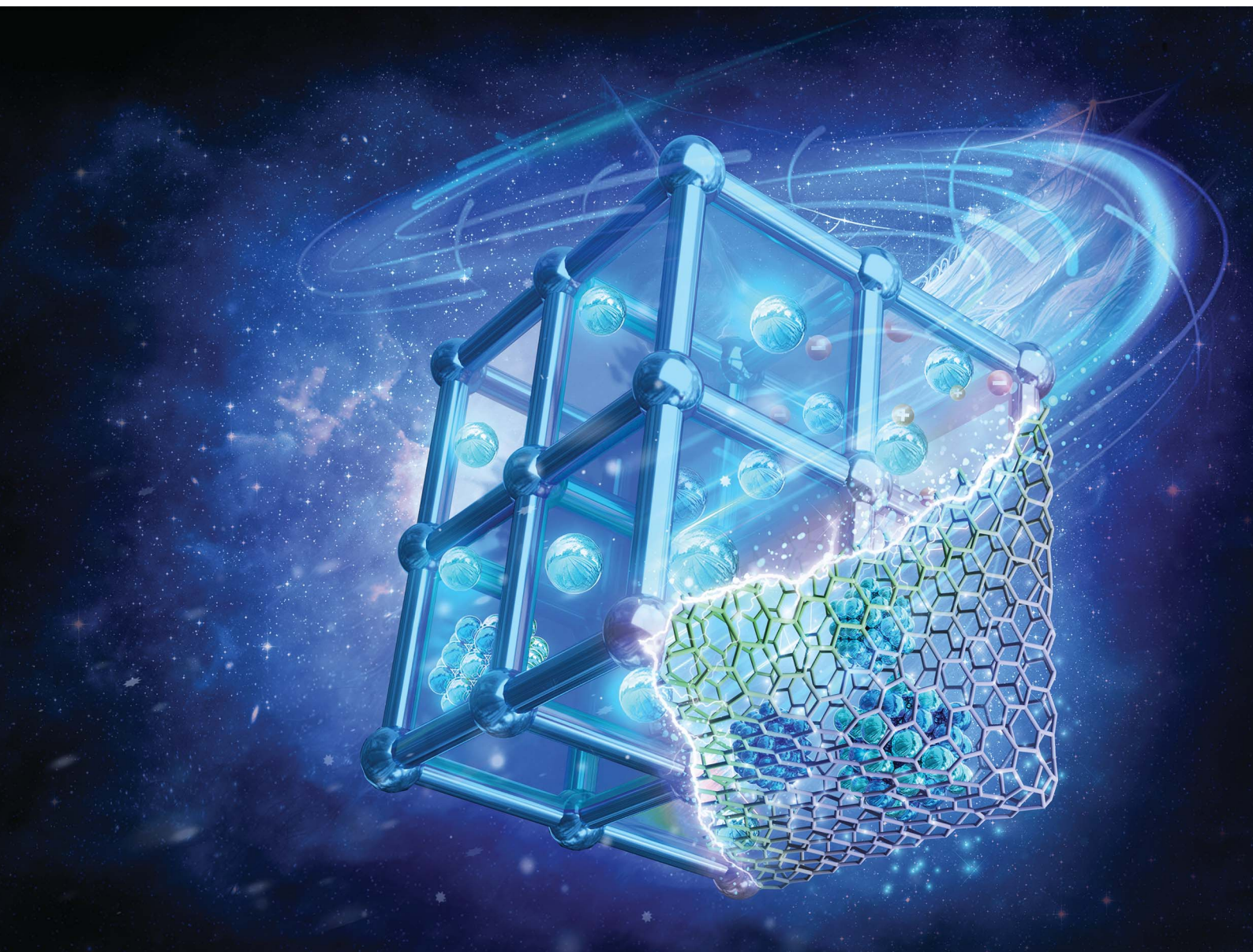


# Chemical Science

Volume 13  
Number 6  
14 February 2022  
Pages 1515–1836

rsc.li/chemical-science



ISSN 2041-6539



## REVIEW ARTICLE

Chun-Ting He *et al.*  
Confinement synthesis in porous molecule-based  
materials: a new opportunity for ultrafine nanostructures

Cite this: *Chem. Sci.*, 2022, 13, 1569

# Confinement synthesis in porous molecule-based materials: a new opportunity for ultrafine nanostructures

Li-Ming Cao,<sup>†</sup> Jia Zhang,<sup>†</sup> Xue-Feng Zhang and Chun-Ting He \*

A balance between activity and stability is greatly challenging in designing efficient metal nanoparticles (MNPs) for heterogeneous catalysis. Generally, reducing the size of MNPs to the atomic scale can provide high atom utilization, abundant active sites, and special electronic/band structures, for vastly enhancing their catalytic activity. Nevertheless, due to the dramatically increased surface free energy, such ultrafine nanostructures often suffer from severe aggregation and/or structural degradation during synthesis and catalysis, greatly weakening their reactivities, selectivities and stabilities. Porous molecule-based materials (PMMs), mainly including metal–organic frameworks (MOFs), covalent organic frameworks (COFs) and porous organic polymers (POPs) or cages (POCs), exhibit high specific surface areas, high porosity, and tunable molecular confined space, being promising carriers or precursors to construct ultrafine nanostructures. The confinement effects of their nano/sub-nanopores or specific binding sites can not only effectively limit the agglomeration and growth of MNPs during reduction or pyrolysis processes, but also stabilize the resultant ultrafine nanostructures and modulate their electronic structures and stereochemistry in catalysis. In this review, we highlight the latest advancements in the confinement synthesis in PMMs for constructing atomic-scale nanostructures, such as ultrafine MNPs, nanoclusters, and single atoms. Firstly, we illustrated the typical confinement methods for synthesis. Secondly, we discussed different confinement strategies, including PMM-confinement strategy and PMM-confinement pyrolysis strategy, for synthesizing ultrafine nanostructures. Finally, we put forward the challenges and new opportunities for further applications of confinement synthesis in PMMs.

Received 29th October 2021  
Accepted 22nd December 2021

DOI: 10.1039/d1sc05983a

rsc.li/chemical-science

## 1. Introduction

Catalysis occupies an extremely important status in industry and is essential for the synthesis of the vast majority of chemicals.<sup>1</sup> The core of catalysis science is the construction of highly active catalysts, and its research has shown phenomenal growth.<sup>2</sup> Metal nanoparticles (MNPs) are a very important class of nanocatalysts due to their abundant reactive surface atoms and special electronic configurations, which have been widely used in heterogeneous catalysis.<sup>2–6</sup> The electronic and crystal structure on the surface of nanomaterials can undergone significant changes. The small size, surface, interface, and macro-quantum tunnelling and quantum size effects make nanomaterials have some excellent properties that traditional materials do not have, such as electromagnetic properties, corrosion resistance, mechanical properties, *etc.*<sup>7</sup> The catalytic properties of MNPs are decisively influenced by their size. Reducing the size of MNPs to the atomic scale can not only

vastly improve the specific surface areas, but also expose abundant catalytically active sites and surface dangling bonds, and/or even distort electronic/band structures.<sup>3</sup> Particularly, ultrafine MNPs (typically < 5 nm) have been confirmed to have attractive catalytic activity and selectivity, as their surface atom ratio can reach up to over 50%, which could enormously change the surface atomic transport and coordination configurations and/or even change the electron spin conformations and the electron spectrum on the surface.<sup>8</sup> Compared with bulk particles, their ultrafine nanostructures provide higher atom utilization, accessible catalytic sites, unique electronic properties, and specific surface/interface configurations, thus leading to superior catalytic reactivity.<sup>3</sup> For example, bulk Au exhibits low reactivity for numerous catalytic reactions, yet exhibits efficient CO oxidation activity at sizes smaller than 5.0 nm.<sup>7</sup> Bulk Pt shows low reactivity in catalytic hydrogenation, but ultrafine Pt NPs (<4.0 nm) demonstrate 100% conversion efficiency.<sup>9</sup> Besides, other important factors determining the activity and selectivity of MNPs are their shape and dispersion. Many studies have shown that the different crystal faces exposed by MNPs exhibit different reactivity. For example, the catalytic rate of the Fe (111) surface surpasses those of its (100) and (110) surfaces by 16 and 418 times, respectively, in the catalytic

Key Laboratory of Functional Small Molecules for Ministry of Education, College of Chemistry and Chemical Engineering, College of Life Science, Jiangxi Normal University, Nanchang 330022, China. E-mail: hct@jxnu.edu.cn

<sup>†</sup> These authors contributed equally.



synthesis of ammonia.<sup>3</sup> For the deoxygenation of aromatic epoxides, the Cu (100) surface exhibits more than 90% conversion, while the Cu (111) surface is only 35%.<sup>10</sup> However, due to the significant increase in surface free energy, ultrafine MNPs often encounter serious aggregation and poor stability during the synthesis as well as catalytic processes.<sup>4</sup> In addition, structural degradation also leads to a precipitous decline in their reactivity and selectivity. Thus, the controllable synthesis of catalytically stable ultrafine MNPs remains a great challenge.

Porous molecule-based materials (PMMs) mainly include metal-organic frameworks (MOFs), covalent organic frameworks (COFs), and porous organic polymers (POPs) or cages (POCs), showing high specific surface areas and high porosity, and more importantly, highly tailorable nano/sub-nano-confined space.<sup>11–23</sup> Thus, PMMs can be used as excellent carriers for confining and stabilizing MNPs.<sup>24–30</sup> Their confinement effect of the nano/sub-nano-pores can not only effectively reduce the agglomeration problem of MNPs, but also can confine the growth of MNPs to obtain ultrafine MNPs.<sup>30</sup> In addition, the confinement metal-organic/organic space can modulate the electronic configuration of MNPs and the host-guest chemistry near the reactive sites, boosting their inherent activity and selectivity.<sup>24</sup> Moreover, PMMs can be used as extremely useful templates/precursors to derive a variety of ultrafine nanostructures, such as nanoclusters or single atom sites through their unique confinement effect.<sup>31</sup> On one hand, PMMs contain a mass of internal nanocages/pores and abundant coordinating atoms, which can isolate metal precursors/metal ions, effectively reducing the diffusion and agglomeration of metals during the pyrolysis process; on the other hand, carbon layers *in situ* derived from PMMs can be electronic regulators and structural stabilizers for atomically dispersed MNPs.

In this review, we will emphasize the current developments in the confinement synthesis in PMMs for synthesizing atomic-scale nanostructures, *e.g.* ultrafine MNPs, nanoclusters, and single atoms. Firstly, we introduced typical confinement methods for the synthesis. Subsequently, we discussed the confinement strategy for fabricating ultrafine nanostructures, including the PMM-confinement strategy and PMM-confinement pyrolysis strategy. Finally, we put forward the challenges faced by PMM-confinement research.

## 2. Confinement methods for synthesis

In fact, it is still a major challenge to embed all MNPs in the nanocages/nanopores of PMMs. This challenge is attributed to the influence of the pore environment, the internal surface characteristics, and the kinetics of wetting and filling of PMMs, which lead to unavoidable loading of some MNPs with uneven size on the surface of PMMs. Generally, the strategies of introducing metal precursors into PMMs mainly include the impregnation method, double-solvent method, chemical vapor deposition method, *in situ* encapsulation method and so on.<sup>25</sup> Subsequently, MNPs can be obtained through various reduction

technologies of metal precursors, such as reduction by using NaBH<sub>4</sub>, hydrogen, ammonia borane, and hydrazine under different conditions.<sup>25</sup>

### 2.1. Impregnation method

Metal precursors can be uniformly inserted into PMMs *via* the impregnation method with the assistance of solvents. Specifically, the homogeneous solution formed by the metal precursors and the PMMs are thoroughly mixed.<sup>32–34</sup> The capillary pressure existing in the system will cause self-infiltration of the solution into the internal spaces of the PMMs. Next, the metal precursors can be easily reduced *in situ* to MNPs without damaging the confinement frameworks. Theoretically, the internal voids of PMMs can absorb all kinds of metal precursors, and after reduction, uniformly dispersed ultrafine MNPs can be obtained. However, sometimes some metal precursors may be loaded (or diffused) outside the PMMs. Because there is no restriction of the nano-spaces, the metal precursors adsorbed on the surface can easily migrate and agglomerate during the reduction process, thus forming MNPs with a larger size and poor dispersion. Therefore, both the PMMs and metal precursors determine the dispersion and particle size of the prepared MNPs. For example, Huang *et al.* inserted Pd NPs into UiO-66 through the solution impregnation method.<sup>34</sup> The activated UiO-66 powder was immersed in methylene chloride containing a certain concentration of palladium acetate. Pd NCs@UiO-66 was prepared by reducing Pd<sup>2+</sup> under a H<sub>2</sub>/Ar flow at a low temperature. The average size of Pd NCs was less than 1.2 nm and they were uniformly dispersed in UiO-66. Dong *et al.* used a COF as a confinement framework to synthesize ultrafine Pd NPs (2–5 nm) by soaking the COF in a methanol solution of Pd(NO<sub>3</sub>)<sub>2</sub>, and subsequently, re-dispersing in water. Then, Pd@COF was constructed by adding NaBH<sub>4</sub>. In addition to crystalline porous materials, amorphous POPs are also suitable for introducing MNPs through this method. For example, Dong *et al.* constructed a POP (PC-POP) by the polymerization of cyanuric chloride and piperazine and introduced Pt<sup>4+</sup> into the pores by immersing it in a methanol solution of chloroplatinic acid.<sup>35</sup> After reduction with H<sub>2</sub> at 250 °C, ultrasmall Pt NPs (2.96 nm) were successfully obtained.

### 2.2. Double-solvent method

In the impregnation method, it is difficult to accurately manipulate the position of MNPs loaded into the internal pores of PMMs. As mentioned above, some metal precursors are probably adsorbed to the external surface of PMMs and easily form agglomerates during the reduction process. An effective alternative strategy is the double-solvent method (DSM), which can be effective in incorporating metal precursors into the voids of PMMs, so as to realize the precise encapsulation of MNPs in their pores without agglomerations.<sup>36–38</sup> The different wettability of PMMs in different solvents is central to the DSM. Normally, hydrophobic organic solvents are employed to disperse hydrophilic PMMs, *e.g.* MOF powders. Then, homogeneous water solution with the dissolved metal precursor is added to the above suspension. Since the hydrophobic organic



solvent and water are immiscible, the metal precursors in the system will form stable droplets, which are introduced into the confined channels by inherent capillary pressure.<sup>25</sup> The ultrafine MNPs are well encapsulated inside the internal pores after reduction, and no large particles are scattered in the external layer of the matrix. For instance, Xu *et al.* proposed the DSM to synthesize MNPs within the MOFs' nanopores devoid of agglomerated MNPs on the crystal interface for the first time.<sup>36</sup> For a typical step, activated MIL-101 powder was soaked in *n*-hexane, and a certain concentration of H<sub>2</sub>PtCl<sub>6</sub>·6H<sub>2</sub>O aqueous solution was added under vigorous stirring. After a solid-liquid separation by filtration and thermal reduction with H<sub>2</sub>, Pt@MIL-101 was prepared with ultrafine Pt NPs of *ca.* 1.8 nm, being obviously larger than the pore windows (1.2–1.6 nm) yet much smaller than the pore diameter (2.9–3.4 nm), indicating that the Pt NPs were well restricted to the isolated apertures of MIL-101 and meanwhile effectively avoided deposition or diffusion to the crystal surface. This method is not limited to the construction of ultrafine single metal NPs. Bimetallic or even multi-metallic alloy NPs can also be perfectly encapsulated inside MOFs by just changing the single metal aqueous solution to a multi-metal one.<sup>37</sup> Since the DSM allows introducing metal ions into the specific pores as well as reducing them *in situ* in such confined spaces, the sizes of the nanoparticles are significantly restricted by the aperture sizes. Dong *et al.* selected two similar triazinyl-COFs called COF-Ph and COF-BPh with different aperture diameters of 2.3 and 3.9 nm, respectively, as confined templates to synthesize Pd NPs through the DSM.<sup>38</sup> The sizes of the resultant Pd NPs were 0.79 and 0.81 nm, respectively, exhibiting strong correlation with that of the corresponding confined templates.

### 2.3. Chemical vapor deposition method

Chemical vapor deposition (CVD) has been applied to construct MNP/PMM composite materials for a long time.<sup>25</sup> This method usually selects organometallic compounds that are easy to sublime at high temperature or have high volatility as metal precursors. Generally, activated PMM powder and volatile metal precursors are packed in two separate bottles and placed together in a Schlenk tube that is kept under vacuum. Volatile organometallic compounds are converted to vapor at a suitable temperature. At this time, PMMs are exposed to metal precursor vapor, which will diffuse into their pores. The speed and extent of the vapor being sucked into the PMMs are determined by the steam pressure. After the final reduction treatment, MNPs can be introduced into PMMs. CVD is a convenient solvent-free process that can load large amounts of MNPs in PMMs. Fischer *et al.* utilized the CVD method to construct ultrafine Pd or Cu NPs (particle sizes of 1–2 nm) loaded inside MOF-5.<sup>39</sup> In a sealed vacuum Schlenk tube, the MOF-5 powder was placed in the vapor of [(η<sup>5</sup>-C<sub>5</sub>H<sub>5</sub>)Cu(PMe<sub>3</sub>)], [(η<sup>5</sup>-C<sub>5</sub>H<sub>5</sub>)Pd(η<sup>3</sup>-C<sub>3</sub>H<sub>5</sub>)], or [(CH<sub>3</sub>)Au(PMe<sub>3</sub>)]. Kempe *et al.* fabricated highly distributed ultrafine bimetallic Pd<sub>x</sub>Ni<sub>y</sub> NPs (*ca.* 2–3 nm) embedded in MIL-101 by CVD with the assistance of dynamic vacuum.<sup>40</sup> The activated MIL-101 powder and metal precursors of [(η<sup>5</sup>-C<sub>5</sub>H<sub>5</sub>)Pd(η<sup>3</sup>-C<sub>3</sub>H<sub>5</sub>)] and [Ni(η<sup>5</sup>-C<sub>5</sub>H<sub>5</sub>)<sub>2</sub>] were positioned in a divided

three-lumen tube, and the system was maintained at 25 °C in a dynamic vacuum of 10<sup>-4</sup> mbar for 3–8 h. The dynamic vacuum can greatly reduce the adsorption of metal precursors to the outer layer of MIL-101. The color of the MOF powder became darker after the metal precursor was adsorbed into the pores. Pd<sub>x</sub>Ni<sub>y</sub>@MIL-101 was finally obtained through a subsequent hydrogenolysis treatment. The CVD method can introduce a variety of metal clusters or even single atoms into specific porous structures or surfaces, but it brings about relatively higher requirements for the selection of metal precursors, and some volatile metal precursors are usually highly toxic, such as some metal carbonyl compounds.

### 2.4. *In situ* encapsulation method

*In situ* encapsulation is considered to be a prospective method for embedding MNPs inside PMMs.<sup>25</sup> Typically, metal precursors are added to the self-assembled system of PMMs. During the crystallization process of PMMs, the metal precursor molecules are encapsulated in the nanocages of PMMs. The frequently used metal precursor molecules mainly include metal acetylacetonate complexes, metal carbonyl compounds, polyoxometalates (POMs) and so on. These metal precursors should have suitable molecular sizes, stable chemical structures, and good solubility in specific solvents. For example, Li *et al.* fabricated polyoxometalate-stabilized single atom site catalysts (SASCs) by the *in situ* encapsulation method.<sup>41</sup> Platinum acetylacetonate Pt(acac)<sub>2</sub> and H<sub>3</sub>PMo<sub>12</sub>O<sub>40</sub> (PMo) were added in the crystallization process of HKUST-1 and the *in situ* encapsulation of Pt(acac)<sub>2</sub> and PMo in its sub-nanopores (~0.9 nm) was realized. Then, Pt<sub>1</sub>-PMo@HKUST-1 was constructed by reducing the metal precursor with 5% H<sub>2</sub> for 1 h at 150 °C. Although this method is relatively simple and often requires only one step reaction to obtain metal precursor loaded PMMs, it is difficult for the metal precursors to be completely wrapped in the process of self-assembly of PMMs in the solution, which will result in the waste of a large amount of metal precursors. The more serious problem is that when using this method, it is usually difficult to accurately control the amount of metal precursor being encapsulated.

## 3. PMM-confinement strategies to synthesize ultrafine nanostructures

Compared with other traditional confinement synthesis strategies (such as zeolite confinement or carbon confinement), PMM-confinement has the following prominent features. Firstly, PMMs can be designed and tailored to exhibit a wealth of versatile structures and morphologies. Secondly, PMMs create a molecular platform for atomic-level control of nano/sub-nano-confined space and functional groups, which can precisely regulate the size, dispersion and microenvironment of MNPs. Thirdly, PMMs are rich in highly ordered micropores (<2 nm), and their spatial confinement effect can realize the synthesis of highly dispersed ultrafine MNPs, nanoclusters or even single atom sites without using surfactants. In addition, PMMs also possess unique pore surfaces. On one hand, the



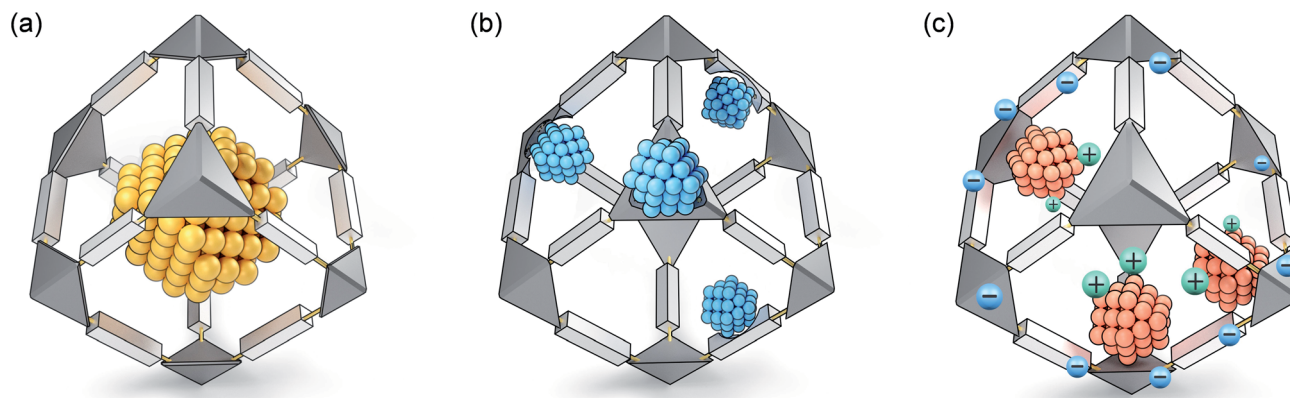


Fig. 1 Three typical PMM-confinement strategies: (a) space-confinement, (b) coordination-confinement and (c) ion-confinement.

coordination-confinement of functional groups can limit the nucleation and growth of MNPs. On the other hand, the functional groups can be used as structural stabilizers and electronic regulators for ultrafine MNPs. Both MOFs and COFs/POPs have their own benefits and drawbacks in confinement synthesis. The significant advantage of MOFs is that they are rich in atomically dispersed metal nodes, which can effectively regulate the electronic structure of MNPs or be synergistically involved in catalysis, thereby promoting the catalytic activity or selectivity of the composite systems. Nevertheless, the chemical stabilities of MOFs are relatively poor, especially in some strongly acidic or basic systems, which limit their applications under such harsh conditions. In contrast, COFs/POPs connected by robust covalent bonds usually have excellent chemical stabilities, showing a wide range of applications in confinement synthesis. The PMM confinement strategy can be divided into three types: space-confinement profiting from the unique nanocage/nanopore construction of PMMs, coordination-confinement through the functional groups on PMMs, decorating N, S, and O with lone pair electrons, and ion-confinement based on the charged PMM skeleton for the electrostatic interaction between anions and cations (Fig. 1). These three kinds of confinement effects can synergistically and significantly inhibit the shifting and clustering of MNPs, enabling the effective preparation of ultrafine nanostructures. In addition, profiting from the structural regularity and site uniformity of PMMs, MNPs can be accurately represented *via* X-ray diffraction, X-ray absorption and/or other spectrum technologies as the active centers of catalysis, which is helpful for the study of the catalytic mechanism.<sup>29</sup>

### 3.1. Space-confinement

**3.1.1. MOFs for space-confinement.** MOFs have an ordered, adjustable, and ultra-small porous structure (<3 nm) and can be used as ideal nanocages to confine ultrafine MNPs in limited space through a “ship-in-a-bottle” method, while preventing their accumulation and restricting their size.<sup>14</sup> The evenly atomically dispersed metal centers and organic functional groups of MOFs themselves can also regulate the surface electronic structures of MNP guests. Cheng and coworkers

incorporated silver ions into activated MIL-101 *via* the solution impregnation method, and then prepared Ag@MIL-101 after reduction with NaBH<sub>4</sub>.<sup>42</sup> Ag NPs possessed a particle size of about  $1.4 \pm 0.4$  nm, which basically matched the nanoporous cavities of MIL-101, indicating that the nanopores in MIL-101 could confine the synthesis of Ag NPs (Fig. 2a). Ag@MIL-101 could efficiently transform CO<sub>2</sub> into propargylic acids bearing terminal alkynes under low temperature (50 °C) and atmospheric pressure conditions. Fischer *et al.* utilized the CVD method to construct Ru NPs in MOF-5 (Ru@MOF-5).<sup>43</sup> The size of Ru NPs was 1.5–1.7 nm, in good agreement with the dimensions of the cavities in MOF-5 (Fig. 2b and c). Ru@MOF-5 could be used as a catalyst for the conversion of benzene to cyclohexane with a yield of approximately 25%. Pd NPs could be selectively encapsulated with MIL-101 of different sizes when Pd(C<sub>5</sub>H<sub>5</sub>)(C<sub>3</sub>H<sub>5</sub>) was introduced by CVD and reduced with H<sub>2</sub> at different temperatures.<sup>44</sup> MIL-101 compliant Pd NPs (2.7 nm) and undersized (1.7 nm) Pd NPs were produced by reduction at room temperature and 70 °C (Fig. 2d). Pd@MIL-101 with 1.7 nm Pd NPs had a higher conversion rate than Pd@MIL-101 with 2.7 nm Pd NPs for larger substrates, since the accessible metal surface was restricted and the interactions with space-critical demanding substrates were reduced when the cavities of the MOF were filled completely. The size of cavities in MOFs and the diameter of confined nanoparticles in the corresponding reported examples of MNPs@MOF are summarized in Table 1.<sup>40,43,45–56</sup> By reasonably adjusting the size of the MOF cavities and the metal precursors, it is even possible to synthesize single-atom catalysts (SACs). For example, Wang *et al.* cleverly constructed a Pd SAC through the space-confinement of a polyoxometalate-based MOF (POMOF).<sup>57</sup> The four SiW<sub>12</sub>O<sub>40</sub><sup>4-</sup> (SiW) anions in POMOF were highly ordered to construct a small cavity (11.76 Å), just enough to wrap a single Pd(acac)<sub>2</sub> molecule (9.1 Å). Benefiting from the gap (6.25 Å) between the two SiW anions which hindered the migration of Pd(acac)<sub>2</sub>, a single-atom Pd catalyst (Pd<sub>1</sub>@Cu-SiW) was constructed through reducing the Pd(acac)<sub>2</sub>@Cu-SiW precursor with H<sub>2</sub> at low temperature. The selectivity of Pd<sub>1</sub>@Cu-SiW for semi-additive hydrogenation of acetylene was as high as 92.6%.



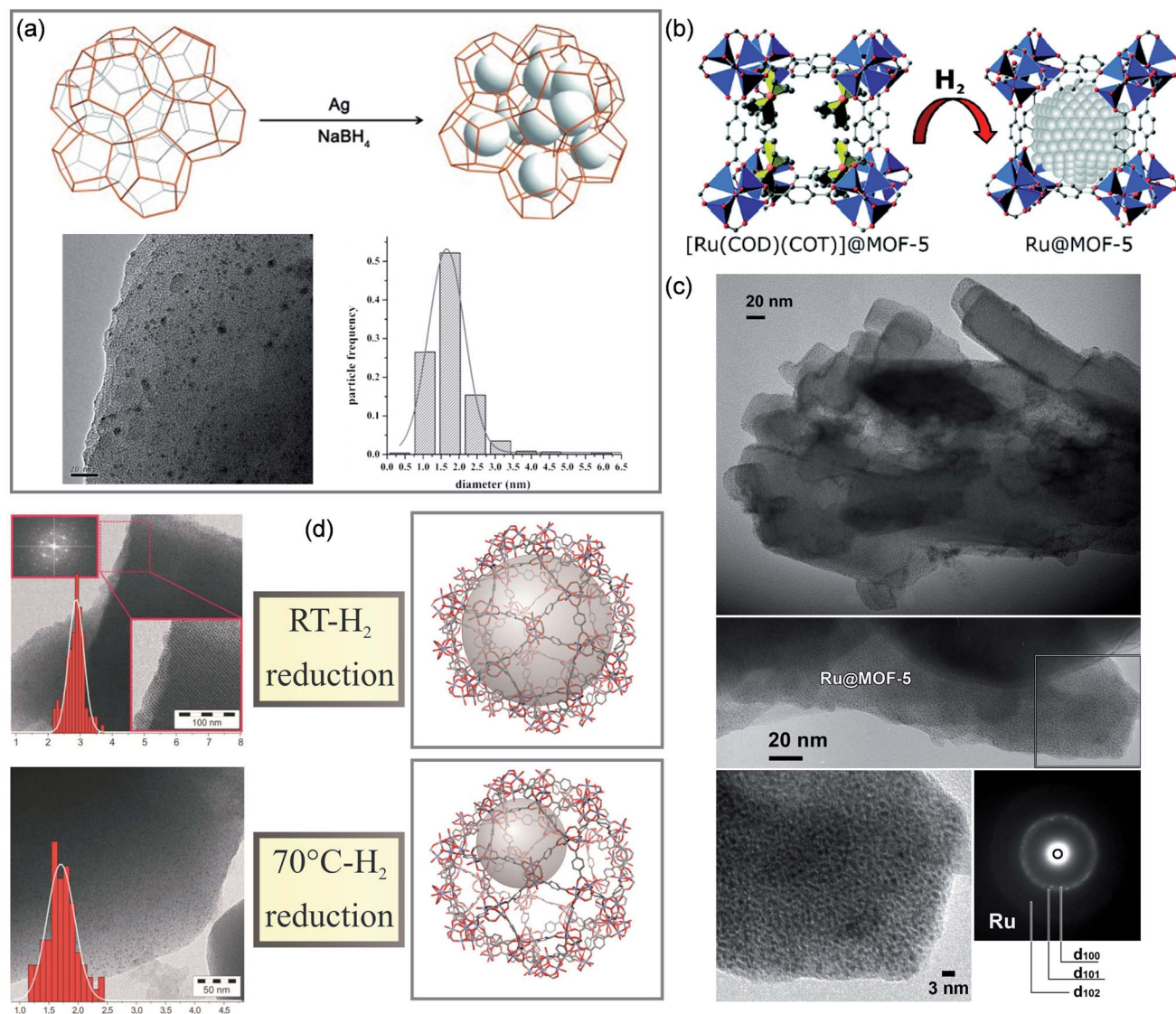


Fig. 2 Cases of MOFs for space-confinement. Synthesis and TEM images of (a) Ag@MIL-101. Reproduced with permission.<sup>42</sup> Copyright 2015, WILEY-VCH. (b and c) Ru@MOF-5. Reproduced with permission.<sup>43</sup> Copyright 2008, American Chemical Society. (d) Pd@MIL-101. Reproduced with permission.<sup>44</sup> Copyright 2011, WILEY-VCH.

**3.1.2. COFs for space-confinement.** COFs, synthesized through condensation reactions between different types of organic monomers, are another class of porous crystalline materials and exhibit structural diversity and high designability.<sup>23</sup> COFs have well-defined pore structures and adjustable aperture diameters and/or morphologies, being perfect for confining the growth of MNPs and realizing the controllable synthesis of ultrafine nanostructures.<sup>58</sup> In addition, COFs are commonly connected by strong covalent bonds and therefore usually possess higher chemical stability, which can be stable for a long time in organic, water, acidic and alkaline solutions.<sup>59</sup>

Jiang *et al.* constructed a TM-TPT-COF with a coordinated nitrogen-rich skeleton *via* using 2,4,6-trimethyl-1,3,5-triazine (TM) and 1,3,5-tris-(4-formylphenyl)-triazine (TPT) as molecular building blocks (Fig. 3a).<sup>60</sup> Its Brunauer–Emmett–Teller (BET) surface area was as high as 810 m<sup>2</sup> g<sup>-1</sup>, and it possessed abundant nanopores, which could restrict the growth of Pt NPs,

thereby preparing highly dispersed ultrafine Pt NPs (*ca.* 2.10 nm). The catalyst showed excellent oxygen reduction reaction (ORR) activity. In 0.1 M HClO<sub>4</sub> solution, the catalytic onset potential and the half-wave potential ( $E_{1/2}$ ) were 1.05 and 0.89 V, respectively. Dong *et al.* synthesized COF-CuTPP through the polymerization of 2-methylpiperazine and copper tetrabromophenolphthalein (Cu-TBrPP) (Fig. 3b). Subsequently, Pd@CCOF-CuTPP was constructed by impregnation and reduction. COF-CuTPP was rich in nanopores, which could limit the growth of Pd NPs. Therefore, the as-prepared Pd NPs (2–5) nm were highly dispersed in COF-CuTPP (Fig. 3c).<sup>61</sup> Pd@CCOF-CuTPP displayed a conversion efficiency of up to 98% in Henry and A<sup>3</sup>-coupling reactions.

**3.1.3. POPs or POCs for space-confinement.** POPs are microporous materials usually constructed from conjugated organic molecular fragments. The abundant micropores in POPs can also effectively confine the growth of MNPs. POPs have the characteristics of adjustable chemical structures and



Table 1 Examples of the reported MNPs@MOF composites with particle sizes fitting the cavity sizes

MOF	Cavity size (nm)	Preparation method	Metal precursor	Reduction method	Particle size (nm)	Ref.
MIL-101	3.0–3.4	Impregnation	Pd(NO <sub>3</sub> ) <sub>2</sub>	H <sub>2</sub>	2.5 ± 0.5	45
		Impregnation	Pd(NO <sub>3</sub> ) <sub>2</sub>	H <sub>2</sub>	2.6 ± 0.5	46
		Impregnation	Pd(NO <sub>3</sub> ) <sub>2</sub>	H <sub>2</sub>	1.9 ± 0.7	47
		Impregnation	Pd(NO <sub>3</sub> ) <sub>2</sub>	Microwave irradiation/ N <sub>2</sub> H <sub>4</sub> ·H <sub>2</sub> O	<3.0	48
		Impregnation	Pd(NO <sub>3</sub> ) <sub>2</sub>	H <sub>2</sub>	2.6 ± 0.5	49
		Impregnation	Pd(acac) <sub>2</sub>	H <sub>2</sub>	2.0–3.0	50
		Impregnation	Pd(NO <sub>3</sub> ) <sub>2</sub>	H <sub>2</sub>	2.0–3.0	51
		Double-solvent	Pd(NO <sub>3</sub> ) <sub>2</sub> and CoCl <sub>2</sub>	NH <sub>3</sub> BH <sub>3</sub>	~2.5	52
		Double-solvent	H <sub>2</sub> PtCl <sub>6</sub>	H <sub>2</sub>	~2.5	53
		Chemical vapor deposition	Pd(C <sub>5</sub> H <sub>5</sub> )(C <sub>3</sub> H <sub>5</sub> )	H <sub>2</sub>	2.7	54
		Chemical vapor deposition	(η <sup>3</sup> -C <sub>3</sub> H <sub>5</sub> )Pd(η <sup>5</sup> -C <sub>5</sub> H <sub>5</sub> ) and Ni(η <sup>5</sup> -C <sub>5</sub> H <sub>5</sub> ) <sub>2</sub>	H <sub>2</sub>	~3.5	40
		Al-MIL-100	2.5–3.0	Impregnation	AgNO <sub>3</sub>	NaBH <sub>4</sub>
		Impregnation	H <sub>2</sub> PtCl <sub>6</sub>	H <sub>2</sub>	1.8 ± 0.4	
UiO-68	2.56	Impregnation	Pd(NO <sub>3</sub> ) <sub>2</sub>	NaBH <sub>4</sub>	<2.0	43
MOF-5	~1.5	Chemical vapor deposition	Ru(cod)(cot)	H <sub>2</sub>	1.5–1.7	56

are easy to design as two-dimensional structures with a high degree of conjugation, which is not only conducive to the improvement of conductivity, but also good for dispersing the active centers and stabilizing the ultrafine MNPs.<sup>62,63</sup> Unlike the network structures described above, POCs are classically zero-dimensional porous materials, exhibiting adjustable confined spaces yet generally good solubility. They can be used to prepare soluble and stable ultrafine MNPs to obtain special nano-

catalytic materials between heterogeneous and homogeneous catalysts.<sup>64–70</sup>

Zhang *et al.* fabricated highly dispersed ultrafine Pd NPs through the space-confinement in a triazinyl-pentaerythritol POP (TP-POP) (Fig. 4a).<sup>71</sup> TP-POP has a wealth of nanopores (pore size of *ca.* 3.0 nm) and excellent structural stability. Pd@TP-POP was prepared by the DSM. Firstly, TP-POP was immersed in H<sub>2</sub>O/CH<sub>2</sub>Cl<sub>2</sub> solution containing Pd(OAc)<sub>2</sub>.

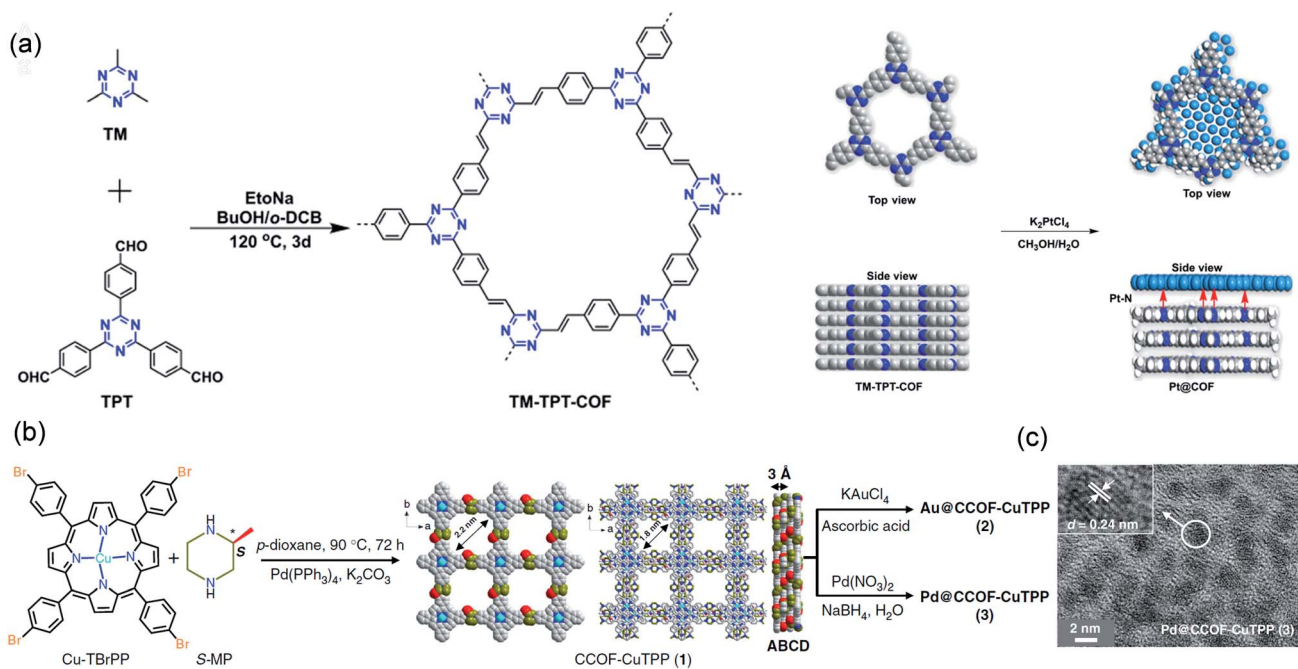


Fig. 3 Cases of COFs for space-confinement. Schematic diagrams of constructing (a) Pt@TM-TPT-COF. Reproduced with permission.<sup>60</sup> Copyright 2020, American Chemical Society. (b) Synthesis and (c) TEM images of Pd@CCOF-CuTPP. Reproduced with permission.<sup>61</sup> Copyright 2019, Springer Nature.



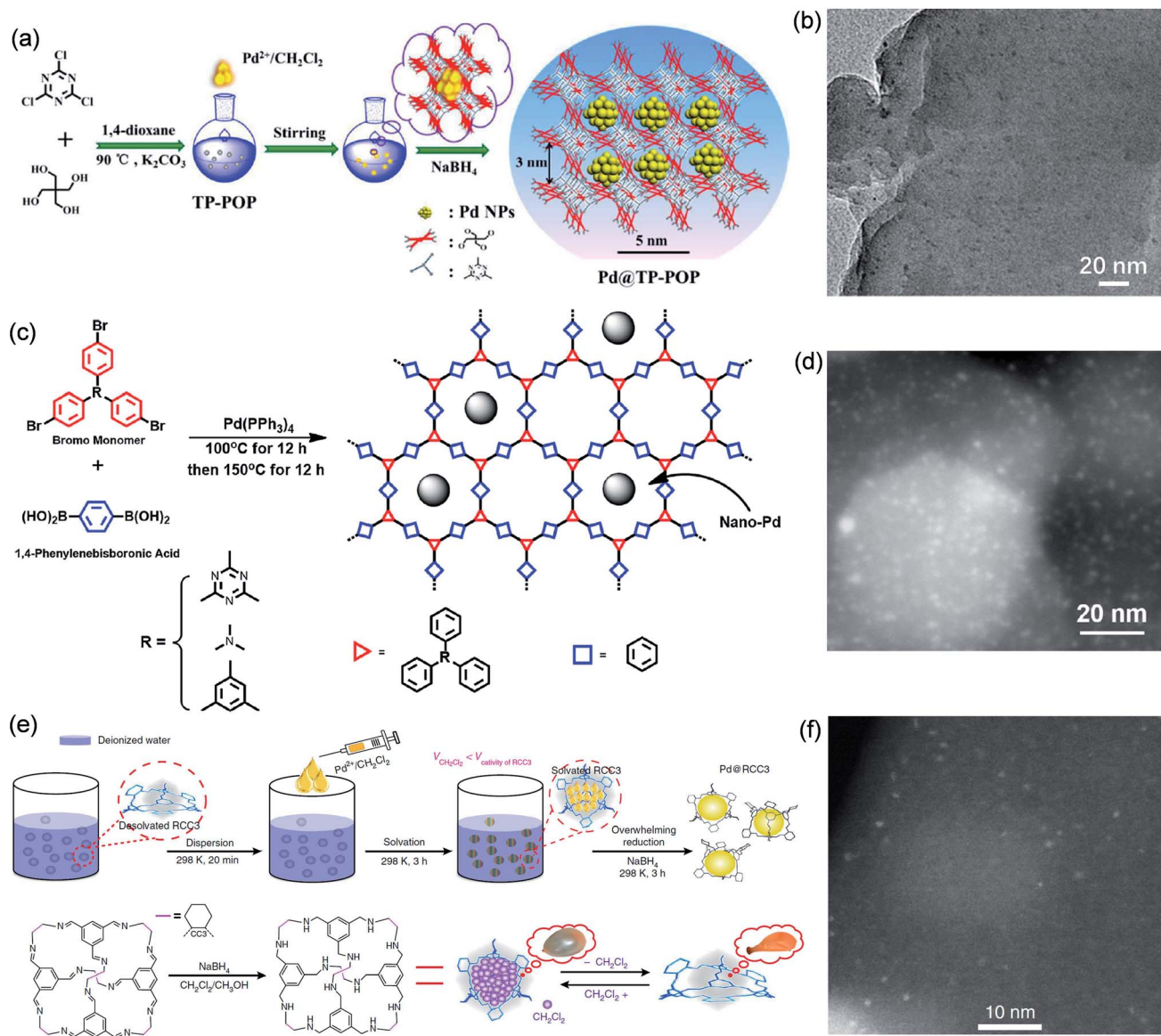


Fig. 4 Cases of POPs or POCs for space-confinement. Construction schematic and TEM images of (a and b) Pd@TP-POP. Reproduced with permission.<sup>71</sup> Copyright 2018, The Royal Society of Chemistry. (c and d) Pd@POP. Reproduced with permission.<sup>72</sup> Copyright 2019, Elsevier. (e and f) Pd@RCC3. Reproduced with permission.<sup>73</sup> Copyright 2018, Springer Nature.

Subsequently, Pd@TP-POP was constructed by reduction with NaBH<sub>4</sub>. These as-constructed Pd NPs exhibited a size range of 1.4–2.8 nm and were highly dispersed in the nanopores of TP-POP instead of appearing in the outer layer (Fig. 4b), indicating that the space-confinement of the nanopores plays a key role. The optimized Pd@TP-POP showed good catalytic properties in the reduction of nitro and aldehyde groups with high convertibility (>98%) and selectivity (100%). Xie *et al.* synthesized ultrafine Pd NPs using a series of microporous POPs (Fig. 4c).<sup>72</sup> Pd(PPh<sub>3</sub>)<sub>4</sub> was employed to facilitate the association of organic bromine monomer and 1,4-phenylenediboronic acid for constructing the POPs. In this process, Pd NPs were formed through the *in situ* transformation of Pd(PPh<sub>3</sub>)<sub>4</sub> and were embedded in the pores of the POPs. Thanks to the restriction of

a large number of nanopores in these POPs, Pd NPs (1.3 nm) presented high dispersion in the organic matrix (Fig. 4d). The ultrafine nanostructures endowed the catalysts with highly exposed catalytic sites, showing outstanding catalytic efficiency in the reduction of *p*-nitrophenol with a conversion rate of up to 99.9%.

Xu *et al.* employed POCs as confinement templates for the synthesis of ultrafine Pd NPs (Fig. 4e).<sup>73</sup> Firstly, the chiral imine cage CC3R was synthesized through the condensation reaction of the organic monomer 1,3,5-triformylbenzene and (*R,R*)-1,2-diaminocyclohexane. Next, the organic molecular cage (RCC3) was prepared by reducing the pre-fabricated CC3R. Since the cage of RCC3 is hydrophobic, they used the DSM to introduce Pd(OAc)<sub>2</sub> into it. Due to the space confinement of the 0.7 nm



organic cages, the prepared Pd nanoclusters encapsulated in the cage have an average diameter of just 0.72 nm (Fig. 4f). They found that the encapsulated Pd nanoclusters not only did not destroy the covalent structure of the cages, but also helped to increase the porosity of RCC3. Confining Pd nanoclusters in the cage cavity could largely reduce particle aggregation and enhance particle stability. Moreover, the Pd nanocluster core was covered by a discrete and soluble RCC3 shell, which exhibited excellent solubility and extremely high dispersibility in solvents, so that it had more accessible metal active centers in the liquid phase reaction. Therefore, Pd@RCC3 exhibited strengthened catalytic efficiency in a variety of reactions, including catalytic hydrogenation of nitroaromatics (up to 100% conversion), hydrogen production of ammonia borane (turnover frequency (TOF):  $176 \text{ min}^{-1}$ ), and reduction of organic dyes.

### 3.2. Coordination-confinement

**3.2.1. MOFs for coordination-confinement.** MOFs are hybrid porous materials with high adjustability both in the metal centers and organic ligands. The organic functional groups rich in lone pairs of electrons in MOFs, such as carboxyl, amino, hydroxyl, *etc.*, can be used to stabilize and confine MNPs since they have strong coordination ability with metal ions. The ordered structure of MOFs makes the anchor points of metal precursors orderly, which is conducive to the uniform distribution of MNPs. Moreover, prior to MOF assembly, the metal precursors can be grabbed by ligands through coordination, avoiding the difficulty of metal precursor diffusion in the MOF pores. Li *et al.* used the 2,2-bipyridine moieties in the bridging

ligand of UiO-67 (2,2-bipyridine-5,5'-terephthalic acid) to immobilize  $\text{Pd}^{2+}$ , and then further synthesized UiO-67 with the Pd cation anchored ligands (Fig. 5a).<sup>74</sup> Finally,  $\text{Pd}^0$ -in-UiO-67 was obtained after  $\text{H}_2$  reduction, with  $3.0 \pm 0.5 \text{ nm}$  Pd NPs distributed uniformly inside the UiO-67 framework. For comparison, the Pd NPs loaded by the traditional impregnation method were mainly on the surface of UiO-67 owning a larger particle diameter of  $5.5 \pm 2.4 \text{ nm}$  (denoted as  $\text{Pd}^0/\text{UiO-67}$ ).  $\text{Pd}^0$ -in-UiO-67 had excellent efficiencies in the reduction of nitrobenzene, aerobic oxidation of alcohols, and olefin hydrogenation, showing better catalytic activity and stability than  $\text{Pd}^0/\text{UiO-67}$ . In addition, they also used  $\text{H}_2\text{bpydc-PdCl}_2$  (4,4'-biphenyldicarboxylic acid coordinated with Pd cations) to exchange with the ligands on the surface of UiO-67 by a solvent assisted ligand exchange-hydrogen reduction (SALE-HR) strategy (Fig. 5b).<sup>75</sup> The much smaller Pd NPs (1.85 nm) can only be encapsulated in the superficial region of UiO-67, which shortened the catalytic mass transfer time, and exhibited excellent catalytic performance in the hydrogenation of nitroarenes.

MOFs not only can be used as stabilizers for MNPs, but also provide a synergistic platform for their functional groups and MNPs to improve the catalytic performances. For instance, Pd NPs were anchored in the apertures of  $\text{NH}_2\text{-MIL-125}$  and  $\text{MIL-125}$  through photo-assisted and ion-exchange digestion approaches ( $\text{Pd-MIL-125}$  and  $\text{Pd-NH}_2\text{-MIL-125}$ ).<sup>76</sup> The introduction of amino groups made the distribution of NPs more uniform, while reducing the size of Pd NPs from 5.5 to 3.1 nm. The  $\text{Pd-NH}_2\text{-MIL-125}$  catalyst exhibited better conversion efficiency than  $\text{Pd-MIL-125}$  for hydrogen generation from formic acid, and the hydrogen production of  $\text{Pd-NH}_2\text{-MIL-125}$  and  $\text{Pd-MIL-125}$  in the

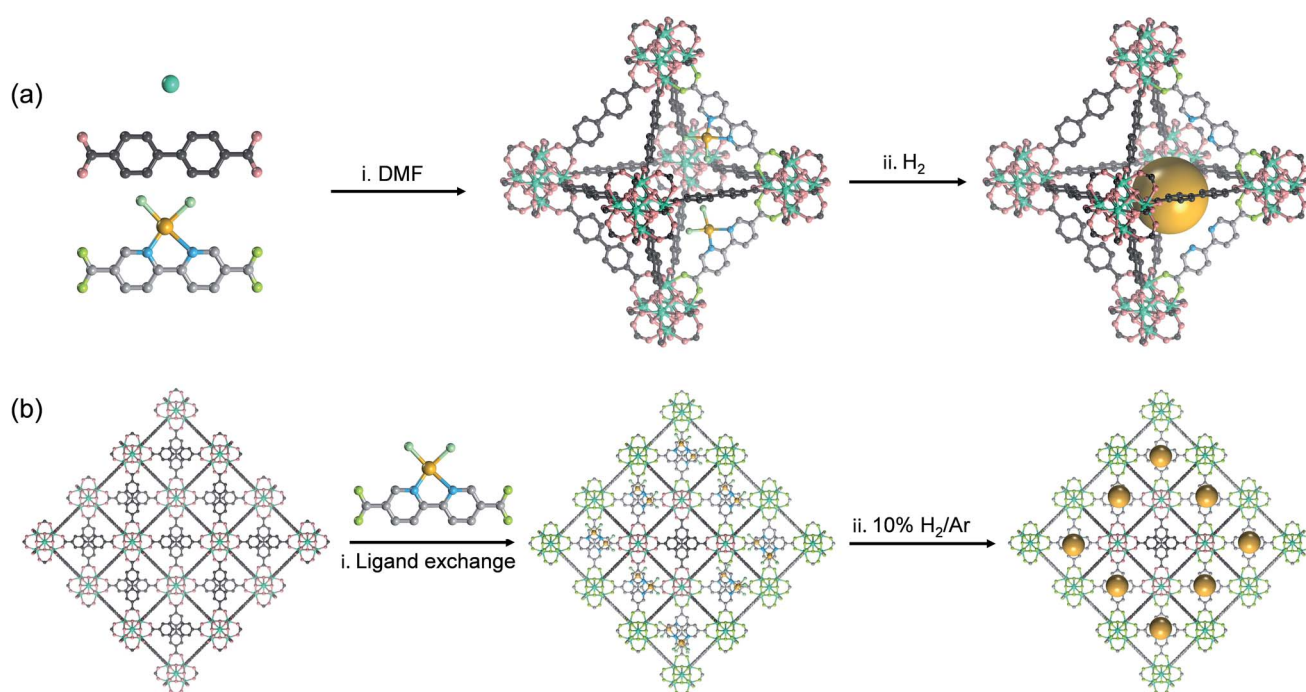


Fig. 5 Cases of MOFs for coordination-confinement. Schematic illustration of constructing (a)  $\text{Pd}^0/\text{UiO-67}$  and (b)  $\text{Pd@UiO-67}$  (C: black or grey, N: blue, O: red or green, Zr: cyan, Cl: purple, and Pd: orange; all the H atoms have been omitted for clarity).



same time was 48.1 and 17.8  $\mu\text{mol}$ , respectively, due to the introduction of amino groups rather than the size of Pd NPs. Being a proton remover, the basic amino groups facilitate the dissociation of the O–H bond by forming  $^{-}\text{H}\text{N}\text{H}_2$  species and benefit the  $\beta$ -hydride elimination from the reaction intermediate. Fei *et al.* successfully encapsulated ultrasmall Au NPs ( $1.8 \pm 0.2$  nm) into an NHC-modified MOF (Au-NC@UiO-68-NHC).<sup>77</sup>  $^{13}\text{C}$  solid-state NMR spectroscopy confirmed that gold precursors can form strong chemical bonds with NHC moieties as nucleation sites, and finally formed ultrafine gold clusters inside the MOF pores through the coordination-confinement. As a control, an amine functionalized MOF was used to load Au NPs under identical conditions (UiO-68-NH<sub>2</sub>/Au), but Au NPs were observed to agglomerate at the outer surface of UiO-68-NH<sub>2</sub> with a size of 5–20 nm, caused by the weak coordination between Au and amine groups. The covalent bonds between Au-NCs and NHCs enhanced their synergistic catalysis with MOFs and effectively promoted charge separation. The LSPR (local surface plasmon resonances) enhanced the light-catalytic CO<sub>2</sub> conversion activity of Au-NC@UiO-68-NHC, with a CO yield of 57.6  $\mu\text{mol g}^{-1} \text{h}^{-1}$ , significantly superior to that of UiO-68-NH<sub>2</sub>/Au (14.3  $\mu\text{mol g}^{-1} \text{h}^{-1}$ ).

If the sizes of the MNPs are reduced to the extreme, single atoms (SAs) can be obtained, where the utilization efficiency of the atoms can reach 100 percent. Since the concept of SACs was put forward in 2011, this type of material has quickly become a hot research topic in the field of catalysis because of their exceptional atom utilization efficiency, controllable coordination environment and outstanding performance, which bridges the homogeneous and heterogeneous catalysis. However, SAs have higher surface energy and more easily migrate and agglomerate than MNPs, and thus the preparation of stable

SACs remains a great challenge. MOFs can stabilize single metal sites through coordination-confinement, which provides an effective strategy to prepare a series of high-activity and reusable heterogeneous SAs@MOF catalysts. SAs@MOF catalysts can be divided into two types according to different single-atom coordination sites: metal node coordination and ligand coordination. Among them, metal nodes that usually serve as Lewis acid sites can create an electron-deficient environment for SAs and regulate their electronic structures. The coordination of SAs to the metal nodes in MOFs can be achieved through three strategies: solvent-assisted ligand incorporation, hydroxyl coordination, and metal ion exchange (Fig. 6). For instance, the Cr<sub>3</sub>( $\mu_3$ -O) node in MIL-101(Cr) can be modified with amines and pyridyl molecules.<sup>78</sup> Nguyen *et al.* modified MIL-101 with dopamine and subsequently interacted with vanadyl acetylacetonate to prepare a vanadium-anchored MOF (V(dop)-MIL-101), and the proportion of V/Cr was about 0.13 determined through ICP-OES (Fig. 6a). V(dop)-MIL-101 showed good conversion efficiency for the oxidation of organic sulfides and could be adjusted to specifically provide the sulfoxide product, and the value of TON to yield sulfoxide and sulfone was 73 and 13, respectively, in the 3rd cycle. NU-1000 was constructed from Zr<sub>6</sub>( $\mu_3$ -O)<sub>4</sub>( $\mu_3$ -OH)<sub>4</sub>(-H<sub>2</sub>O)<sub>4</sub>(OH)<sub>4</sub> (abbreviated to Zr<sub>6</sub>) and 1,3,5,8-(*p*-benzoate) pyrene. The hydroxyl groups enriched in the metal nodes could coordinate with bis(*tert*-butylimido)bis(dimethylamino)molybdenum(vi) (Mo(am)<sub>2</sub>(im)<sub>2</sub>) through thermal deposition, and after coming into contact with oxygen for full oxidation, molybdenum(vi) oxide was placed on the Zr<sub>6</sub> node (denoted as Mo-SIM).<sup>79</sup> Mo(vi) atoms were coordinated with oxygen-containing functional groups in Zr<sub>6</sub>, and ICP-OES analysis revealed 2.8 Mo per Zr<sub>6</sub> (Fig. 6b). Mo-SIM achieved 93  $\pm$  2% conversion in

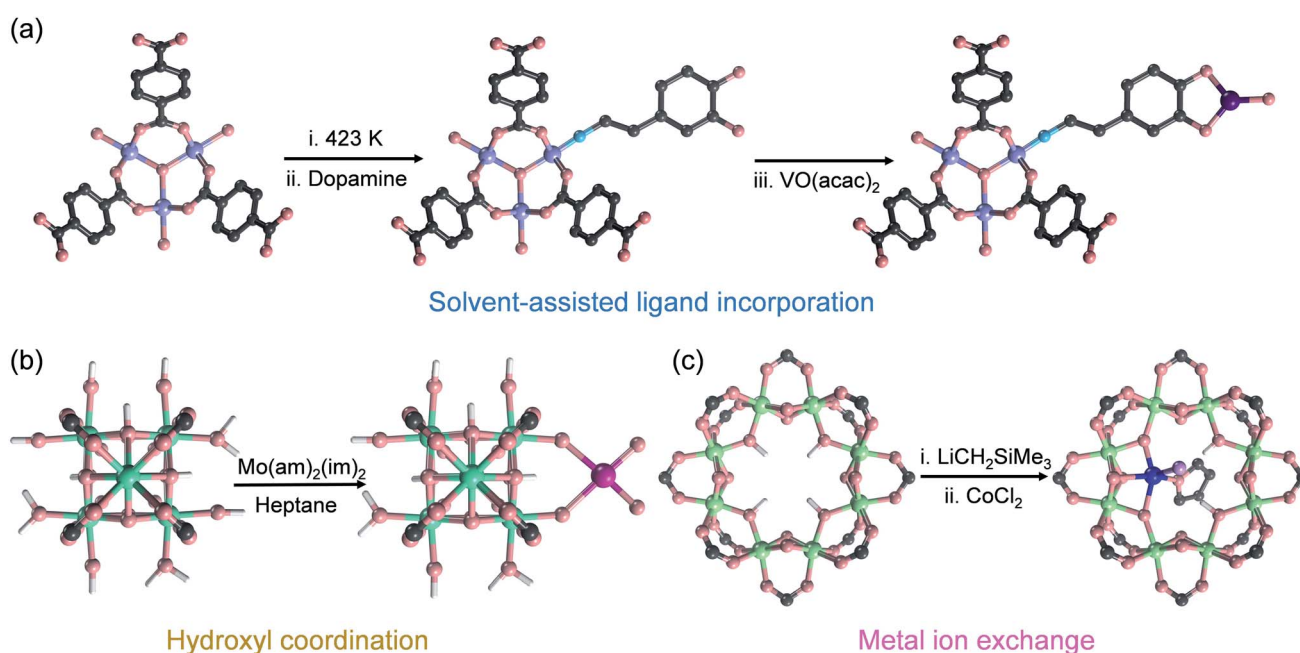


Fig. 6 The confinement strategies for SAs to the metal nodes in MOFs: (a) solvent-assisted ligand incorporation (H atoms have been omitted for clarity), (b) hydroxyl coordination and (c) metal ion exchange (C: black, N: blue, O: red, Cr: violet, Zr: cyan, Al: green, V: purple, Mo: magenta, Ti: olive, Cl: light pink, and H: white).



catalyzing cyclohexene epoxidation. As nodes of the  $\text{Ti}_8\text{-BDC}$  MOF,  $\text{Ti}_8(\mu_2\text{-O})_8(\mu_2\text{-OH})_4$  can coordinate with  $\text{Co}^{2+}$  through ion exchange after  $\text{Ti}_8\text{-BDC}$  was deprotonated with  $\text{LiCH}_2\text{SiMe}_3$ .<sup>80</sup> ICP-MS analysis revealed the presence of 0.7 Co per  $\text{Ti}_8$  node in this single-site Co catalyst named  $\text{Ti}_8\text{-BDC-CoCl}$ .  $\text{Ti}_2^{\text{III}}\text{Ti}_6^{\text{IV}}\text{-BDC-CoH}$  was further prepared from  $\text{Ti}_8\text{-BDC-CoCl}$  with  $\text{NaBH}_4$  treatment, which has high catalytic activity for the hydrogenation of various heteroarenes (Fig. 6c). The yields of  $\text{Ti}_2^{\text{III}}\text{Ti}_6^{\text{IV}}\text{-BDC-CoH}$  for the hydrogenation of pyridine, hindered pyridines (including 2,6-lutidine and 2,4,6-collidine), and quinoline derivatives (such as 3-methylquinoline and 2,6-dimethylquinoline) were all over 90%.

Salicylaldimine-, monophosphine-,  $\beta$ -diketimine-, and bipyridine-based ligands have a strong binding affinity to metals, which is beneficial for stabilizing single metal sites. At the same time, strategies such as post-synthesis modification, solvent-assisted linker exchange, and post-synthetic deprotection are conducive to the synthesis of such SAs@MOF catalysts (Fig. 7). Wang *et al.* reported that copper ions could be captured on the ligands of UiO-66- $\text{NH}_2$  by  $-\text{NH}_2$ , and Cu SAs were further anchored on MOFs ( $\text{Cu SAs/UiO-66-NH}_2$ ) after a photoinduced process (Fig. 7a).<sup>81</sup> Cu SAs/UiO-66- $\text{NH}_2$  can promote the reduction of carbon dioxide as an excellent photocatalyst, with the conversion rates of carbon dioxide to methanol and ethanol of 5.33 and 4.22  $\mu\text{mol h}^{-1} \text{g}^{-1}$ . Fontecave *et al.* exchanged the partial ligand of UiO-67 (bpydc, 2,2'-bipyridine-5,5'-dicarboxylic acid) with  $\text{Cp}^*\text{Rh}(\text{bpydc})\text{Cl}_2$  ( $\text{Cp}^*$  = pentamethylcyclopentadiene) to generate a novel MOF loaded with rhodium SAs ( $\text{Cp}^*\text{Rh@UiO-67}$ ) (Fig. 7b).<sup>82</sup>  $\text{Cp}^*\text{Rh@UiO-67}$  can be used as a photosensitive catalyst to convert  $\text{CO}_2$  to

formate with a TOF of 7.5  $\text{h}^{-1}$ , and it could be recycled up to 6 times. Lin *et al.* modified NacNac ( $\beta$ -diketiminate) in  $\text{Zr}_6\text{O}_4(\text{OH})_4(\text{TPDC-NH}_2)_6$ , an amino-functionalized UiO-type MOF, by reaction with amino groups. They further utilized NacNac to coordinate with metal ions and then reduction with  $\text{NaBH}_4$  to exploit NacNac-M-MOF ( $\text{M} = \text{Fe}, \text{Cu}$  and  $\text{Co}$ ) (Fig. 7c).<sup>83</sup> NacNac-Fe-MOF, NacNac-Cu-MOF, and NacNac-Co-MOF can catalyze the hydrogenation of alkenes, amination of alkyl azides, and amination of cyclohexene, respectively. Wang *et al.* synthesized a Cu SAC by utilizing the coordination-confinement of N-heterocyclic carbene (NHC) encapsulated in UiO-67.<sup>84</sup> Firstly, the NHC (1,3-dibenzyl-1H-imidazole-3-ium bromide,  $2\text{Bn}\cdot\text{HBr}$ ) molecule was *in situ* encapsulated in UiO-67 ( $2\text{Bn@UiO-67}$ ), thanks to the perfect size-matching between the UiO-67 cavity and  $2\text{Bn}\cdot\text{HBr}$ . Subsequently, a single-atom site Cu catalyst ( $2\text{Bn-Cu@UiO-67}$ ) was constructed through the coordination of Cu and carbene C.  $2\text{Bn-Cu@UiO-67}$  exhibited excellent electrocatalytic performance for the conversion of  $\text{CO}_2$  to  $\text{CH}_4$  with a Faraday efficiency of 81%.

**3.2.2. COFs for coordination-confinement.** COFs can be easily functionalized *via* post-modification or bottom-up synthesis of various functional groups like hydroxyl groups, sulfonic acid groups, phosphoric acid groups, amino groups, and thiol/thioether groups. The functionalized side chains can anchor and confine the growth of MNPs, thereby improving the binding ability to metal ions or MNPs and facilitating the preparation of highly dispersed ultrafine MNPs.<sup>85–92</sup> Furthermore, coordination atoms also can act as electronic regulators, which have been confirmed to contribute significantly to catalytic reactions.

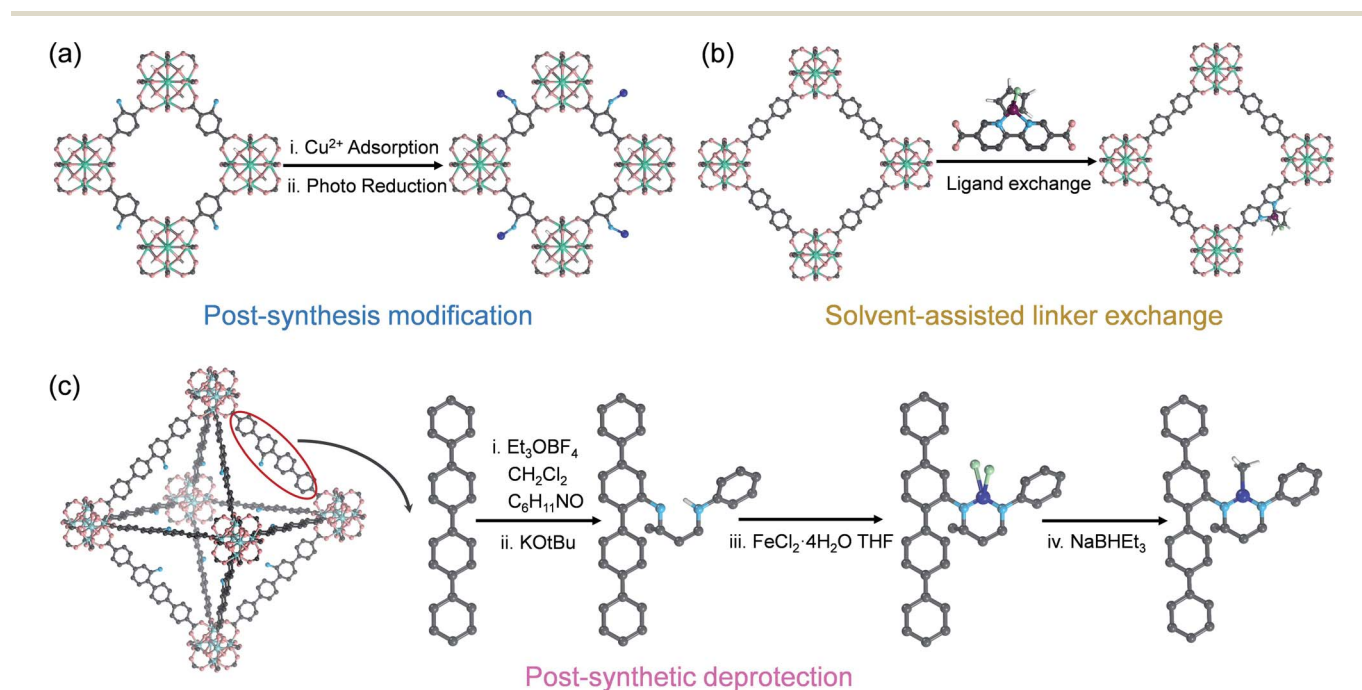


Fig. 7 The confinement strategies for SAs to the ligands in MOFs: (a) post-synthesis modification, (b) solvent-assisted linker exchange and (c) post-synthetic deprotection (C: grey, N: blue, O: red, Zr: cyan, Cu: orange, Rh: wine, Cl: green, and Fe: dark blue; the H atoms on the frameworks have been omitted for clarity).



Thiol/thioether groups have good coordination ability, can anchor a variety of metals, and are often modified to the side chains of COFs to confine the synthesis of MNPs and improve their catalytic activity and stability.<sup>93</sup> Lu *et al.* successfully modified thiol chains in the COF channel using a post-modification synthesis strategy (Fig. 8a).<sup>94</sup> Thanks to the strong binding force between  $-SH$  and Au, the thiol group in the pore could act as a nucleation site for Au NPs and limit the growth of Au nanoclusters. The as-prepared Au NPs with a very small diameter of 1.8 nm were uniformly distributed in Au@COF-S-SH. In contrast, the Au nanoclusters on COF-V (without thiol chain modification) tended to agglomerate with a larger size (Fig. 8b). Moreover, photoelectrochemical experiments and calculation of binding energy had shown that Au-S-COF bridging can improve the charge separation efficiency and keep Au nanoclusters highly dispersed under long-term light exposure. Therefore, Au@COF-S-SH exhibited enhanced performance and stability in the photodegradation of Rhodamine B. Zhang *et al.* constructed a thioether-containing COF (Thio-COF) *via* a bottom-up synthesis strategy, and then highly dispersed ultrafine Pt NPs (1.7 nm) and Pd NPs (1.78 nm) were synthesized by coordination-confinement from the thioether groups in the COF (Fig. 8c and d).<sup>95</sup> Both PtNPs@Thio-COF and

PdNPs@Thio-COF exhibited significant conversion efficiency (>95%) in reducing nitrophenol.

Nitrogen atoms can not only provide lone-pair electrons, but also have relatively small electronegativity and easily give electrons. Therefore, they have strong coordination ability and can coordinate with many kinds of metal ions. Amino groups and imines are also often used to anchor and limit the nucleation and growth of MNPs.<sup>96–102</sup> For instance, Yue *et al.* adopted a COF possessing amine groups (COF-300) to confine the synthesis of ultrafine Pd NPs for benzyl alcohol oxidation.<sup>103</sup> They prepared three different COFs *via* controlling the molar ratio of tetrakis(4-anilyl)methane (TAM) and terephthalaldehyde (TPA) and studied the confinement effects of the three COFs on Pd NPs. With the optimized proportion of TAM and TPA, the prepared COF-300-1114 showed the best confinement effect. The size of the highly dispersed ultrafine Pd NPs was just 1.58 nm. The formation of ultrafine nanostructures was because when the organic monomer TAM increased, an excessive number of suspended amino groups could be introduced, which could act as nucleation sites for Pd and limited their migration and agglomeration during the reduction process. Pd/COF-300-1114 showed a good catalytic effect and stability for benzyl alcohol oxidation with a rather high conversion rate of 97% and

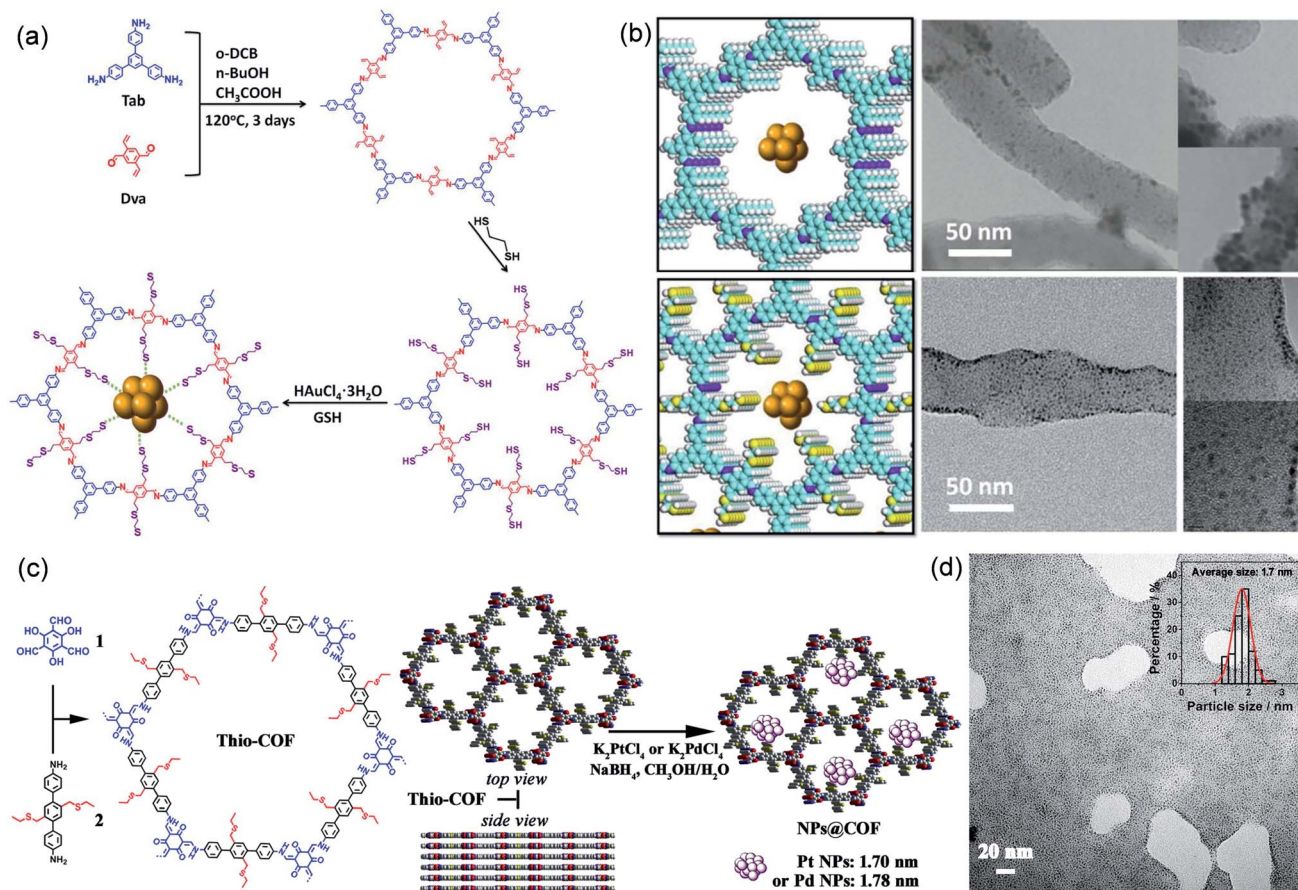


Fig. 8 Cases of COFs for coordination-confinement. Construction schematic and TEM images of (a and b) Au@COF-S-SH. Reproduced with permission.<sup>94</sup> Copyright 2020, WILEY-VCH. (c and d) Pt NPs@Thio-COF. Reproduced with permission.<sup>95</sup> Copyright 2017, American Chemical Society.



selectivity as high as 99%. The high activity of Pd/COF-300-1114 was attributed to the existence of amino groups, which stabilized the Pd NPs and accelerated their activity through amino donor electrons.

Phosphine groups have high binding affinity to various metal ions and are widely used as organic ligands to prepare metal-organic compounds. The ordered phosphine groups introduced into COFs can not only anchor metal ions or MNPs, but also make the metal sites uniformly dispersed in the COF. For instance, Zhang *et al.* fabricated a phosphine-based COF (Phos-COF-1) for the first time and used its phosphine coordination site to control the synthesis of a series of highly dispersed ultrafine MNPs.<sup>104</sup> Because triphenylphosphine (PPh<sub>3</sub>) has good binding affinity to various metal ions, the orderly distributed PPh<sub>3</sub> functional groups in porous Phos-COF-1 can supply nucleation sites for MNPs. Attributed to the coordination and restriction of PPh<sub>3</sub> in Phos-COF-1, the average

sizes of the as-prepared Pd, Pt and Au were 1.62, 2.06, and 1.78 nm, respectively, and they were highly dispersed and evenly distributed in Phos-COF-1. MNPs@Phos-COF-1 showed good transformation efficiency in the reduction of 1-bromo-4-nitrobenzene and nitrophenol, coupling reaction, and tandem coupling and reduction of nitroiodobenzene. Moreover, MNPs@Phos-COF-1 was easy to recycle and can well maintain the nanostructure as well as high stability.

**3.2.3. POPs or POCs for coordination-confinement.** 1,2,3-triazolyl can coordinate with a variety of metal ions and is therefore often employed to manipulate the construction of MNPs.<sup>105,106</sup> For example, Wang *et al.* constructed two types of POPs comprising 1,2,3-triazolyl (CPP-Y and CPP-C) *via* a Yamamoto coupling reaction and click reaction, and discussed the influence of different synthesis routes on their structure and activity (Fig. 9a).<sup>107</sup> The coordination of 1,2,3-triazolyl with Pd and the spatial restriction of POP channels effectively limited

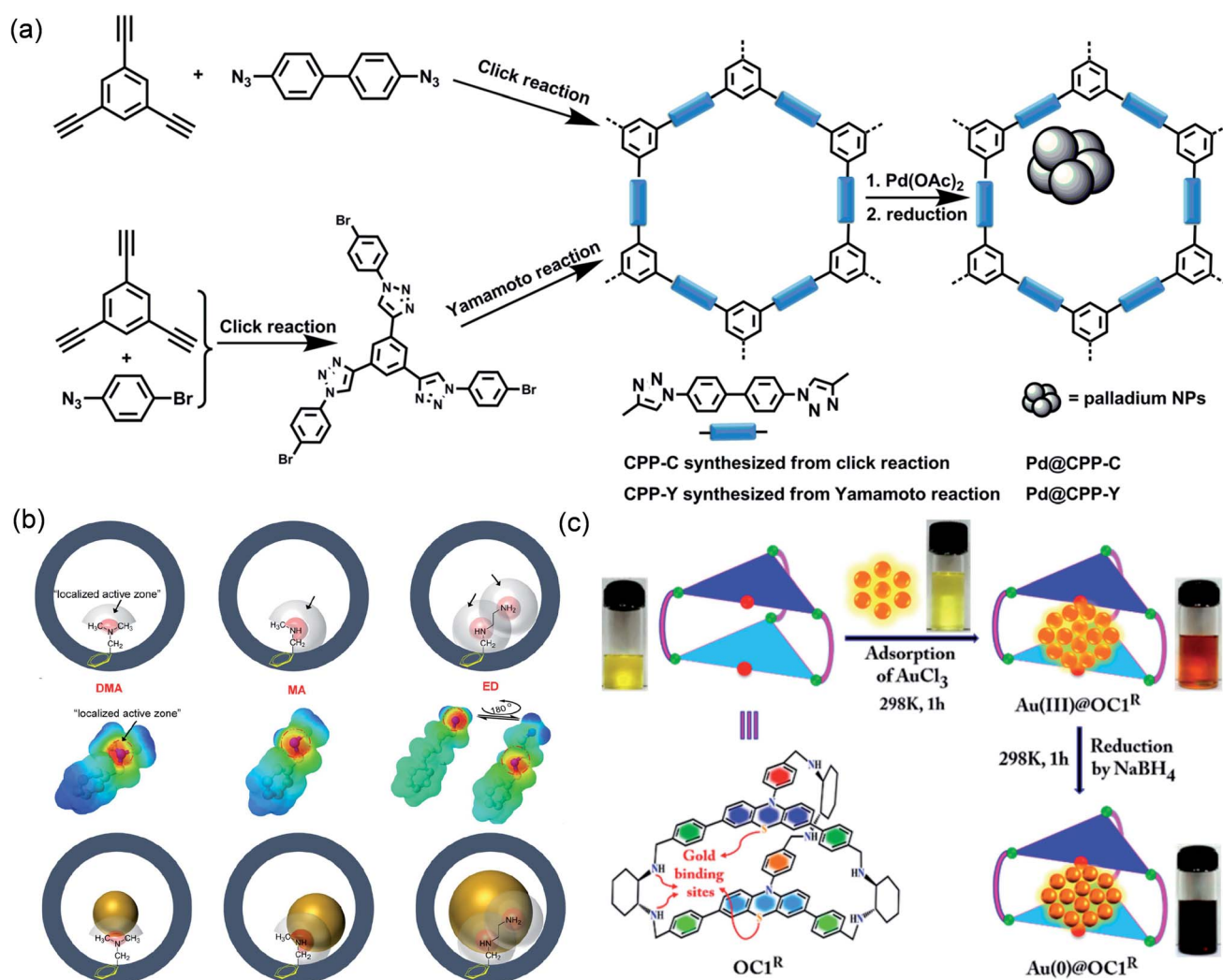


Fig. 9 Cases of POPs or POCs for coordination-confinement. Schematic illustration of constructing (a) Pd@CPP-Y or Pd@CPP-C. Reproduced with permission.<sup>107</sup> Copyright 2015, American Chemical Society. (b) Ag@OMP-DMA, Ag@OMP-MA, or Ag@OMP-ED. Reproduced with permission.<sup>114</sup> Copyright 2019, American Chemical Society. (c) Au@OC1R. Reproduced with permission.<sup>119</sup> Copyright 2017, American Chemical Society.



the growth of Pd NPs, thereby constructing highly dispersed ultrafine nanostructure. The average size of Pd NPs in Pd@CPP-Y and Pd@CPP-C was 1.39 and 1.69 nm, respectively, which could expose more catalytically active sites. Moreover, 1,2,3-triazolyl anchored Pd NPs could improve the stability of the catalysts. Therefore, Pd@CPP-Y exhibited good catalytic activity for olefin hydrogenation reactions with 100% conversion efficiency, and the conversion still surpassed 90% after being recycled 7 times.

The electron-rich amino group can coordinate with a variety of metal ions and is also often used for the confinement-synthesis of MNPs.<sup>108–113</sup> Studies have found that the spatial site resistance and electron-giving capability of the amino substituents also affect the construction of MNPs. Wu *et al.* fabricated three different types of amino-functional ordered mesoporous polymers (OMP-DMA, OMP-MA, and OMP-ED), and explored their effects on the confinement-synthesis of Ag NPs (Fig. 9b).<sup>114</sup> The aminos can be coordinated with Ag<sup>+</sup>, and their different types determine the activity range of their coordination. They called the enriched electron zones near N the “localized active zones (LAZs)”. The properties of LAZs

depended on the substituents' site resistance and electron-giving capability. They found that modified electron-rich amines regulated the growth of Ag NPs by creating LAZs. As the extent of the LAZ surrounding N increased, excess Ag was confined to the area, which led to producing non-uniform larger MNPs. The DMA exhibited the smallest LAZ due to the presence of two –CH<sub>3</sub> with the largest steric hindrance. Therefore, the average size of Ag NPs synthesized by OMP-DMA, OMP-MA and OMP-ED was 6, 9, and 11 nm, respectively. Moreover, they synthesized NH<sub>2</sub>-functionalized OMP (NOMP) through a bottom-up synthesis strategy. Because –NH<sub>2</sub> had a smaller LAZ volume, the average size of Ag NPs in the as-synthesized Ag@NOMP was only 3–4 nm. Thus, the yield of Ag@NOMP in converting alkynes into alkynyl carboxylic acids reached more than 95%.

Upon introducing a variety of electron-rich coordination atoms into the organic cage, the coordination-confinement can cooperate with the space-confinement of the organic cage to limit the growth of MNPs.<sup>115–118</sup> Mukherjee *et al.* reported the use of an organic cage OC1R to synthesize ultrafine Au NPs as a heterogeneous photocatalyst (Fig. 9c).<sup>119</sup> Calculations showed

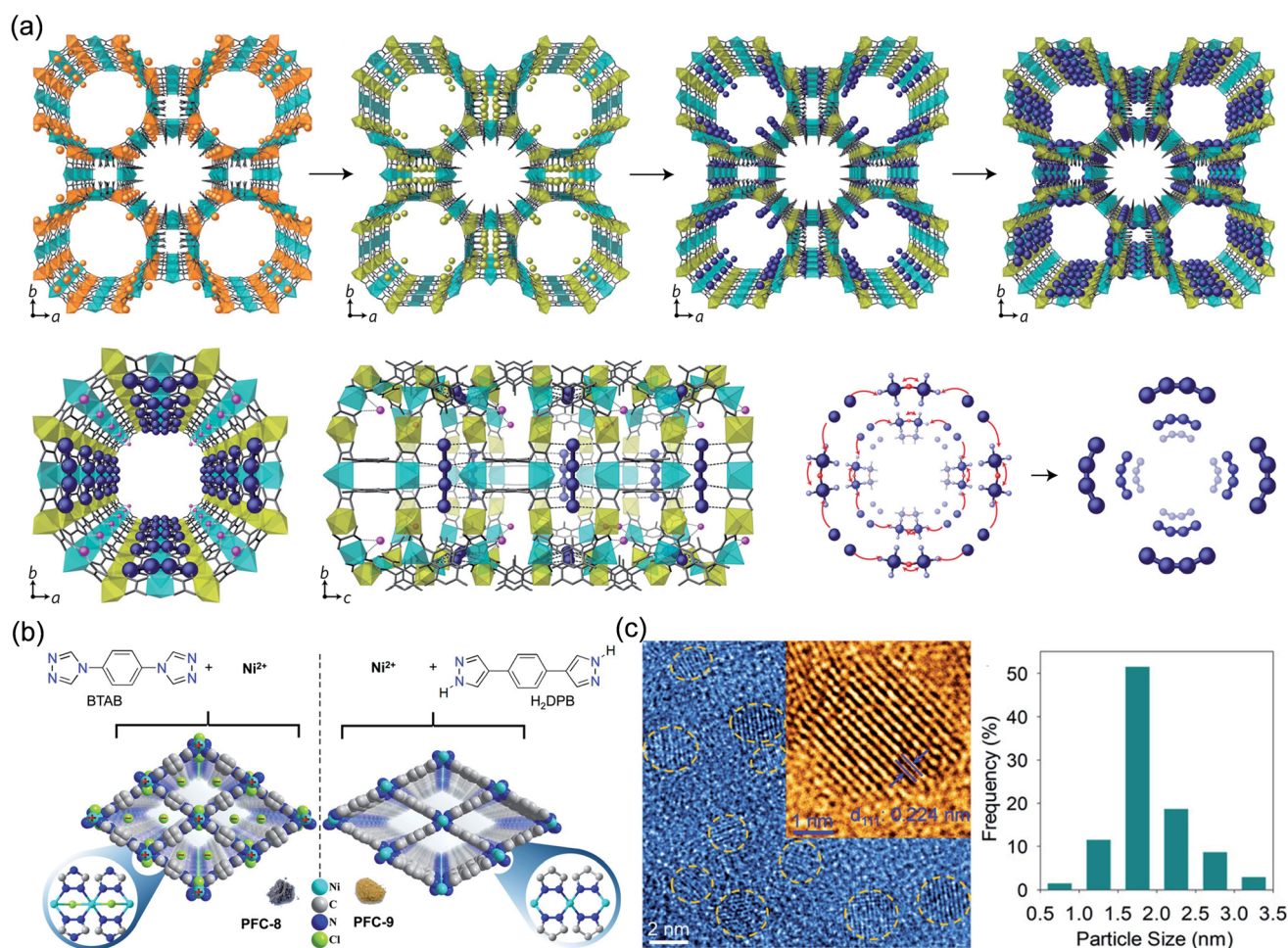


Fig. 10 Cases of MOFs for ion-confinement. (a) Synthesis and X-ray crystal structure of Pd<sub>4</sub><sup>0/1+</sup>-MOF. Reproduced with permission.<sup>120</sup> Copyright 2017, Springer Nature. (b) Schematic representation of the structures of cationic PFC-8 and neutral PFC-9. (c) HRTEM images and Pd particle size distribution of Pd@Nano-PFC-8. Reproduced with permission.<sup>121</sup> Copyright 2020, WILEY-VCH.



that the cavity size of OC1R was between 1.67 and 1.82 nm. OC1R contained vicinal diamine clefts and cyclic thioether moieties, in which electron-rich N and S can coordinate with  $\text{Au}^{3+}$  to provide nucleation sites for Au NPs and stabilize metal active centers. The average particle size of the prepared ultrafine Au NPs was *ca.* 2.0 nm.  $^1\text{H}$  diffusion-ordered spectroscopy (DOSY) NMR revealed that free cages OC1R and  $\text{Au}@OC1\text{R}$  had similar diffusion coefficients, indicating that OC1R and  $\text{Au}@OC1\text{R}$  had comparable shapes and sizes, thus confirming that each Au NP was anchored in a single cage cavity instead of being combined by multiple cages. In addition, they found that the loading of Au in  $\text{Au}@OC1\text{R}$  was as high as 68 wt% without agglomeration. In contrast, when Au loaded by other methods reaches 20 wt%, significant agglomeration of MNPs will often occur. The formation of highly dispersed ultrafine nanostructures was attributed to not only the space-confinement of the ultrafine nanocage, but also the coordination-confinement of abundant N and S atoms.  $\text{Au}@OC1\text{R}$  can be used as a photocatalyst for the selective reduction of nitroaromatics to azo compounds, showing over 99% conversion and over 90% selectivity. Moreover,  $\text{Au}@OC1\text{R}$  exhibited excellent structural stability and reusability, and even though it was repeatedly used 5 times, there was no agglomeration of Au NPs.

### 3.3. Ion-confinement

**3.3.1. MOFs for ion-confinement.** The skeleton of a few special ionic MOFs is charged, and the metal precursor can be replaced into the MOF cages through ion exchange. The charged MOF skeleton can confine and stabilize the metal ions and protect them from agglomeration through the interaction of anions and

cations.  $\text{Mg}_2^{\text{II}}[\text{Mg}_4^{\text{II}}[\text{Cu}_2^{\text{II}}(\text{Me}_3\text{mpba})_2]_3] \cdot 45\text{H}_2\text{O}$  is a highly porous anionic MOF (Me<sub>3</sub>mpba refers to *N,N'*-2,4,6-trimethyl-1,3-phenylenebis(oxamate)).  $\text{Mg}^{2+}$  in this MOF can be replaced by  $\text{Ni}^{2+}$  through ion exchange to obtain  $\text{Ni}_2^{\text{II}}[\text{Ni}_4^{\text{II}}[\text{Cu}_2^{\text{II}}(\text{Me}_3\text{mpba})_2]_3] \cdot 54\text{H}_2\text{O}$ .  $\text{Ni}^{2+}$  was further exchanged with  $[\text{Pd}^{\text{II}}(\text{NH}_3)_4]^{2+}$  and then reduced with  $\text{NaBH}_4$  to obtain  $\text{Pd}_4^{0/+1}$ -MOF (denoted as  $[\text{Pd}_4]_{0.5}@\text{Na}_3[\text{Ni}_4^{\text{II}}[\text{Cu}_2^{\text{II}}(\text{Me}_3\text{mpba})_2]_3] \cdot 56\text{H}_2\text{O}$ ). The Pd<sub>4</sub> cluster has 2 units of positive charge ( $[\text{Pd}_4]^{2+}$ ) and can be well-dispersed and solidified by the skeleton of the anionic MOF (Fig. 10a).<sup>120</sup> Therefore,  $\text{Pd}_4^{0/+1}$ -MOF can effectively catalyze carbene mediated reactions, while can be collected and recycled without the depletion of the catalytic activity with time. PFC-8 and PFC-9 have identical coordination bonds, spatial groups and topological structures, but PFC-8 is a cationic MOF and PFC-9 is a neutrally charged MOF. Profiting from the positively charged skeleton of PFC-8,  $[\text{PdCl}_4]^{2-}$  ions can be evenly dispersed in PFC-8 through an ion exchange process. Then Pd@Nano-PFC-8 (PFC-8 supported Pd NPs with a diameter of 1.75 nm) can be prepared after being reduced with  $\text{NaBH}_4$  (Fig. 10b). Under the same conditions, the ion exchange process of PFC-9 was much slower since without the electrostatic force, which cause inhomogeneous Pd NPs primarily presented surrounding PFC-9 (Pd@PFC-9). Pd@Nano-PFC-8 showed high conversion efficiency and selectivity (>99%) in catalytic H<sub>2</sub> generation from formic acid with  $\text{TOF}_{\text{Pd}} = 5141 \text{ h}^{-1}$ , and the activity did not significantly decrease after 5 consecutive reactions. In contrast, the  $\text{TOF}_{\text{Pd}}$  and conversion rate of Pd@PFC-9 were only  $2443 \text{ h}^{-1}$  and 32.7%, respectively. The structure of Pd@PFC-9 was destroyed after one reaction and lost its catalytic performance.<sup>121</sup>

**3.3.2. POPs or POCs for ion-confinement.** Ionic POPs or POCs also can exhibit strong electrostatic attraction to

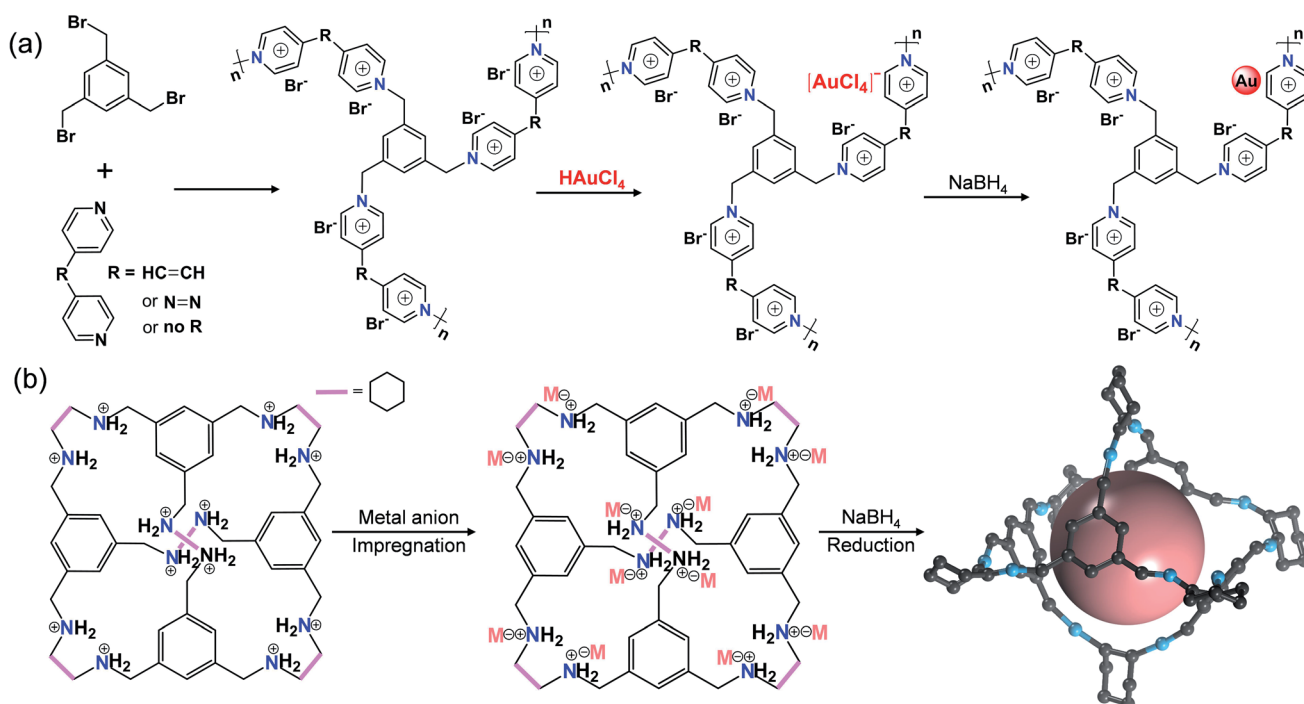


Fig. 11 Cases of POPs or POCs for ion-confinement. Schematic illustration of constructing (a)  $\text{Au}@PION$  and (b)  $\text{MCs}@I\text{-Cage-Cl}$ .



oppositely charged guest species and therefore are also used to anchor and stabilize MNPs.<sup>122–126</sup> Dai *et al.* synthesized high ion-density PIONs (nanoporous ionic organic networks) through the nucleophilic substitution reaction between the organic monomers 1,3,5-tris(bromomethyl)-benzene and 1,2-bis(4-pyridyl)ethylene (Fig. 11a).<sup>127</sup> Since  $\text{AuCl}_4^-$  ions can be uniformly anchored in PIONs by the electrostatic effect through ion exchange,  $\text{Au@PION}$  was prepared after reduction with  $\text{NaBH}_4$  with a Au NP size of *ca.* 1–2 nm and uniformly dispersed in the pores.  $\text{Au@PION}$  presented high conversion efficiency (>99%) and selectivity (>99%) for the oxidation of saturated alcohols. Yuan *et al.* fabricated ionic organic cages by acidifying the neutral amine cage RCC3 with hydrochloric acid (I-Cage-Cl) (Fig. 11b).<sup>128</sup> The high cation density, coulombic attraction and confinement effect in the ion cages promoted the uniform anchoring of the guest anion  $[\text{AuCl}_4]^-$  in I-Cage-Cl. Finally,  $\text{Au@I-Cage-Cl}$  was prepared after reduction, and the size of Au NPs was *ca.* 0.65 + 0.2 nm. Various ultrafine precious metal clusters (MCs) can be prepared in the interior of I-Cage-Cl, benefiting from the positive charge-rich cage that can capture metal-containing negative ions to control the growth of MNPs. Therefore,  $\text{MCs@I-Cage-Cl}$

exhibited high activity and recyclability in the liquid phase  $\text{NH}_3\text{BH}_3$  (AB) hydrolysis reaction.

#### 4. PMM-confinement pyrolysis to synthesize ultrafine nanostructures

Through the preparation of ultrafine nanostructures by pyrolysis of metal-containing precursors, it is easy to obtain thermodynamically stable crystal phases or to obtain phases that can only be formed at higher temperature, such as metal carbides, nitrides, *etc.* Commonly used synthesis strategies include direct metal precursor pyrolysis, mechanical mixed pyrolysis of metal ions and small organic molecules, high temperature vapor deposition, *etc.* However, through these methods it is often difficult to control the morphology and particle size of MNPs, and some methods encounter cumbersome operations or high costs. Therefore, the strategy of using PMMs as confinement templates has attracted attention in recent years due to their excellent adjustability and confinement effect.<sup>129–131</sup> According to the structural features and confinement characteristics of PMMs, the confinement pyrolysis strategy can be divided into space-confinement pyrolysis (SCP) and coordination-confinement pyrolysis (CCP) (Fig. 12). In the PMM-

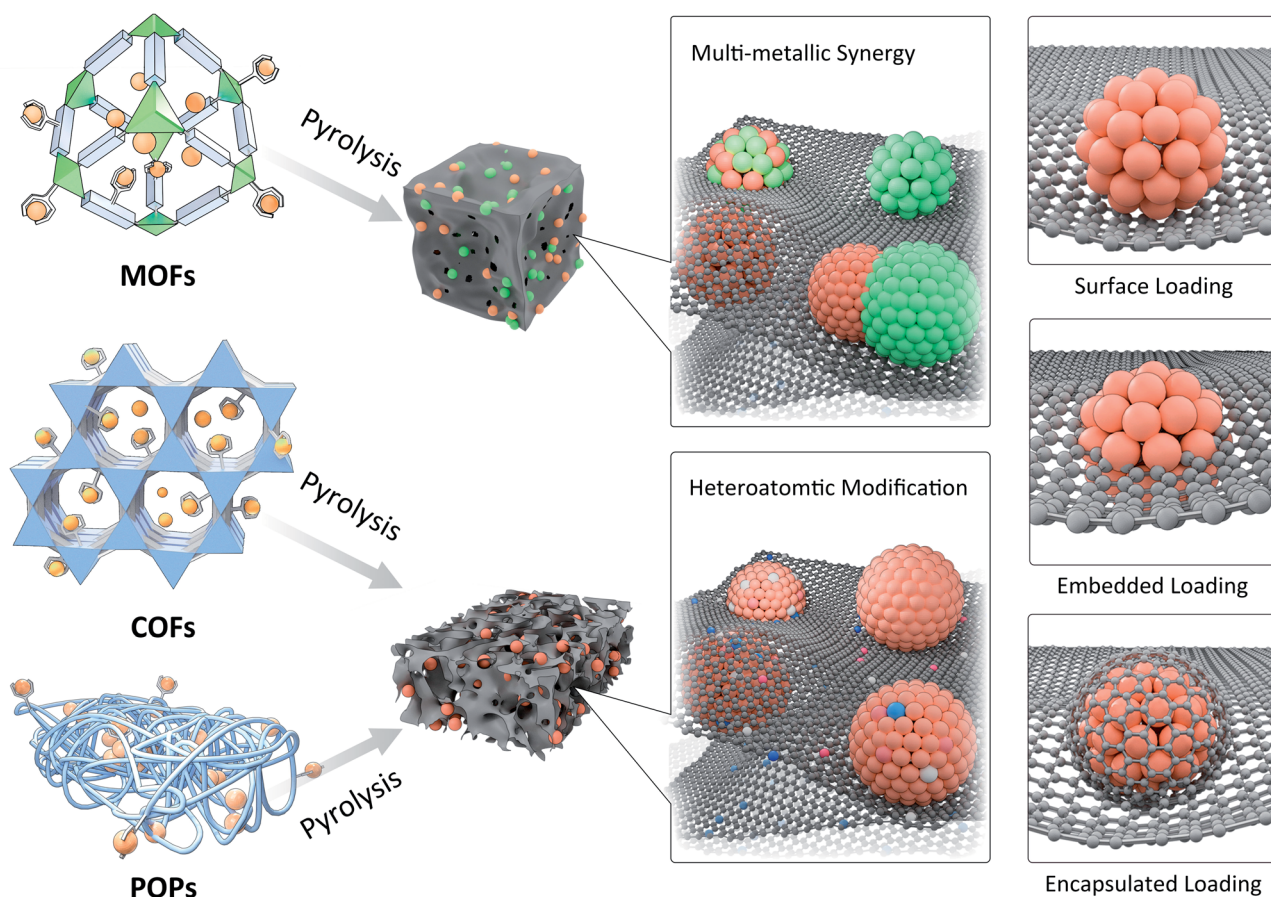


Fig. 12 Confinement pyrolysis of MOFs, COFs, or POPs to synthesize ultrafine nanostructures with controllable compositions and atomic structures.



confinement pyrolysis, an effective strategy to control the synthesis of ultrafine MNPs or SAs is to precisely regulate the ratios of PMM hosts to metal precursor guests. Besides, modulating the pyrolysis conditions (*e.g.* temperature, time, atmosphere, *etc.*) can also play important roles. Moreover, it is necessary to reveal the structures of ultrafine MNPs or SAs. Generally, the crystal structure, microscopic morphology, chemical composition, and bonding information of MNPs can be obtained by conventional powder X-ray diffraction (PXRD), transmission electron microscopy (TEM), X-ray photoelectron spectroscopy (XPS), Raman spectroscopy and Fourier-transform infrared spectroscopy (FT-IR) techniques. X-ray absorption spectroscopy (XAS) and aberration-corrected scanning transmission electron microscopy (AC-STEM) can be helpful to identify single atom sites.

#### 4.1. Space-confinement pyrolysis

The SCP strategy is the use of nanocages/pores or bulky building blocks of PMMs to confine or isolate the metal precursor and then block its aggregation at high temperature.<sup>132</sup> According to the different space types of PMMs, SCP can be divided into hybrid space-confinement pyrolysis (HSCP) and organic space-confinement pyrolysis (OSCP). Typically, MOFs are constructed from ligands and metal centers, which can provide organic-inorganic hybrid nano-space to confine guest molecules with suitable size based on host-guest chemistry. When the scale of the guest exactly matches the size of the nanocages and the pore windows of MOFs, each guest molecule is firmly confined in a separate nanocage, effectively avoiding their diffusion/agglomeration during the pyrolysis process. Besides, the other significant advantage of the HSCP is that additional metal elements from the hybrid frameworks can be purposefully introduced into the final materials. During the pyrolysis process, the metal atoms contained in MOFs can be doped into MNPs or form a heterostructure with them. On one hand, a large number of studies have confirmed that doping foreign metal atoms into the lattice of MNPs can significantly adjust the coordination and electronic structure of the active atoms, thereby adjusting their catalytic performance. On the other hand, heterostructures are beneficial to charge separation and interfacial charge transfer, provide more catalytic sites, and achieve synergistic catalytic effects, so that they exhibit unique properties in catalytic reactions. In comparison, COFs and POPs have abundant nanopores connected by organic monomers through covalent bonds and/or secondary bonds. The pre-designed nanopores in COFs or POPs can also isolate metal precursors and reduce their migration and agglomeration during the pyrolysis process, thereby forming ultrafine MNPs. Therefore, using the organic space in COFs or POPs to control the preparation of ultrafine MNPs is a typical OSCP strategy.<sup>133</sup> The most significant advantage of this strategy is that it is particularly easy to introduce heteroatoms into the resultant materials. Generally, organic monomers are highly modifiable and can be decorated with various heteroatoms. Thus, these heteroatoms can be uniformly introduced into COFs or POPs through the polymerization reaction of organic monomers.

During the pyrolysis process, these heteroatoms can be uniformly doped into the derived carbon supports or MNPs. For one thing, heteroatom-doped carbon can provide additional active sites, and for another, heteroatom doping into MNPs can also regulate the electronic structure of the metal centers, thereby regulating their catalytic activity. Furthermore, the carbon derived from PMMs can be both an electronic regulator and a structural stabilizer for atomically dispersed metal nanomaterials.

**4.1.1. Hybrid space-confinement pyrolysis.** The key to using nanocages in host frameworks to control the synthesis of ultrafine MNPs by pyrolysis is to select host and guest molecules with perfectly matched sizes. The size of the selected guest molecule is smaller than the cavity diameter of the nanocage in the host, but larger than the pore window size. It ensures that the guest molecules can be wrapped in the cavity yet cannot easily migrate out of the pores of the host, thereby isolating and confining the guest molecules.<sup>134</sup> The nanocage size of MOFs is highly adjustable and can be adjusted by regulating the organic ligands as well as metal nodes. Moreover, many MOFs have good structural stability and can exist stably in water, acidic solutions, alkaline solutions and/or various organic solvents without destroying the porous architectures. Therefore, MOFs with good structural stability are often used as the host molecules. The frequently used guest molecules mainly include metal acetylacetonate complexes, metal carbonyl compounds, POMs and so on.<sup>135–137</sup> These guest molecules have a suitable molecular size and stable chemical structure and easily form homogeneous solutions.

The unique HSCP of MOFs can introduce additional metals to strengthen the catalytic properties of MNPs. Teng *et al.* constructed Pd-Cu NPs wrapped with porous N-doped carbon *via* such a strategy (Pd-Cu/PNC).<sup>138</sup> A Cu-BTC (BTC = 1,3,5-benzenetricarboxylic acid) octahedral crystal with nano-scale cavities was selected as the host molecule. Palladium acetylacetonate (Pd(acac)<sub>2</sub>) was selected as the guest molecule, which could enter the Cu-BTC nanocavities through immersion and capillary force. After pyrolysis, Pd-Cu/PNC was prepared (Cu NPs: ~30 nm and Pd NPs: 2.0 nm). The formation of ultrafine Pd NPs was attributed to the space-confinement, which can reduce the migration and agglomeration of Pd precursors. Pd-Cu/PNC exhibited great denitrification, with a nitrate removal rate of about 97.1% and N<sub>2</sub> selectivity of about 83%. In contrast, Cu/PNC without Pd exhibited rather poor denitrification, with a nitrate removal rate of only 62% and a N<sub>2</sub> selectivity of only 28%. In addition, commercial Pd/C and porous carbon had worse effects on denitrification (<20%). These experimental results confirmed that Pd-Cu/PNC had high performance for denitrification on account of the cooperative catalysis of Pd nanoclusters and Cu NPs derived from the MOF metal nodes.

MAF-4 (also called ZIF-8) has an adjustable crystal morphology and a highly ordered porous structure. It is considered a promising precursor for the synthesis of well-defined nanocatalysts and is used as a good host molecule to control the synthesis of ultrafine MNPs, due to a relatively large cavity yet a small window.<sup>139</sup> In addition, the carbon support derived from MAF-4 has a high specific surface area and porous



characteristics. For instance, Li *et al.* adopted a host-guest strategy to prepare a series of single metal atoms ( $M_1/CN$ ) through HSCP (Fig. 13a).<sup>139</sup> Taking the construction of  $Ir_1/CN$  as an example, MAF-4 and  $Ir(acac)_3$  were selected as the host and guest molecules, respectively. Because the diameter of  $Ir(acac)_3$  ( $d_i = 9.8 \text{ \AA}$ ) is exactly between the ZIF-8 aperture ( $d_p = 3.4 \text{ \AA}$ ) and the cavity diameter ( $d_c = 11.6 \text{ \AA}$ ),  $Ir(acac)_3$  molecules can be engaged in the cavities of MAF-4 without migrating out of the pores, realizing the effect of space-confinement, thereby avoiding the migration and accumulation of metal in pyrolysis. Extended X-ray absorption fine structure (EXAFS) illustrated that Ir was well dispersed on the CN substrate in the form of single atoms. Least-squares FT-EXAFS fitting of  $Ir_1/CN$  confirmed that the Ir center was four-coordinated and the average bond length is  $2 \text{ \AA}$ . The X-ray absorption near-edge

structure (XANES) confirmed that the oxidation state of Ir was between 0 and +4.  $Ir_1/CN$  exhibited excellent activity for electrocatalytic formic acid oxidation, with mass activity reaching  $12.9 \text{ A mg}_{Ir}^{-1}$ . A wide range of SACs (Pd, Pt, Ru, Cu, Ni, Mo, Ga, and Mn) could be prepared using this HSCP strategy.

Wang *et al.* constructed atomically dispersed uniform  $Ru_3$  clusters through the confinement of molecular cages in MAF-4.<sup>140</sup>  $Ru_3(CO)_{12}$  was selected as the guest molecule, because its diameter is about  $8.0 \text{ \AA}$ , so it can be contained in a cage without being released. XANES, EXAFS, and wavelet transform (WT) confirmed the existence of Ru-N, Ru-Ru and Ru-C in  $Ru_3/CN$ , and the atom-dispersed  $Ru_3$  clusters were stabilized by nitrogen in the carbon layer.  $Ru_3/CN$  exhibited a good catalytic effect in the oxidation reaction of 2-aminobenzyl alcohol, with the conversion rate and chemoselectivity reaching 100%. The TOF

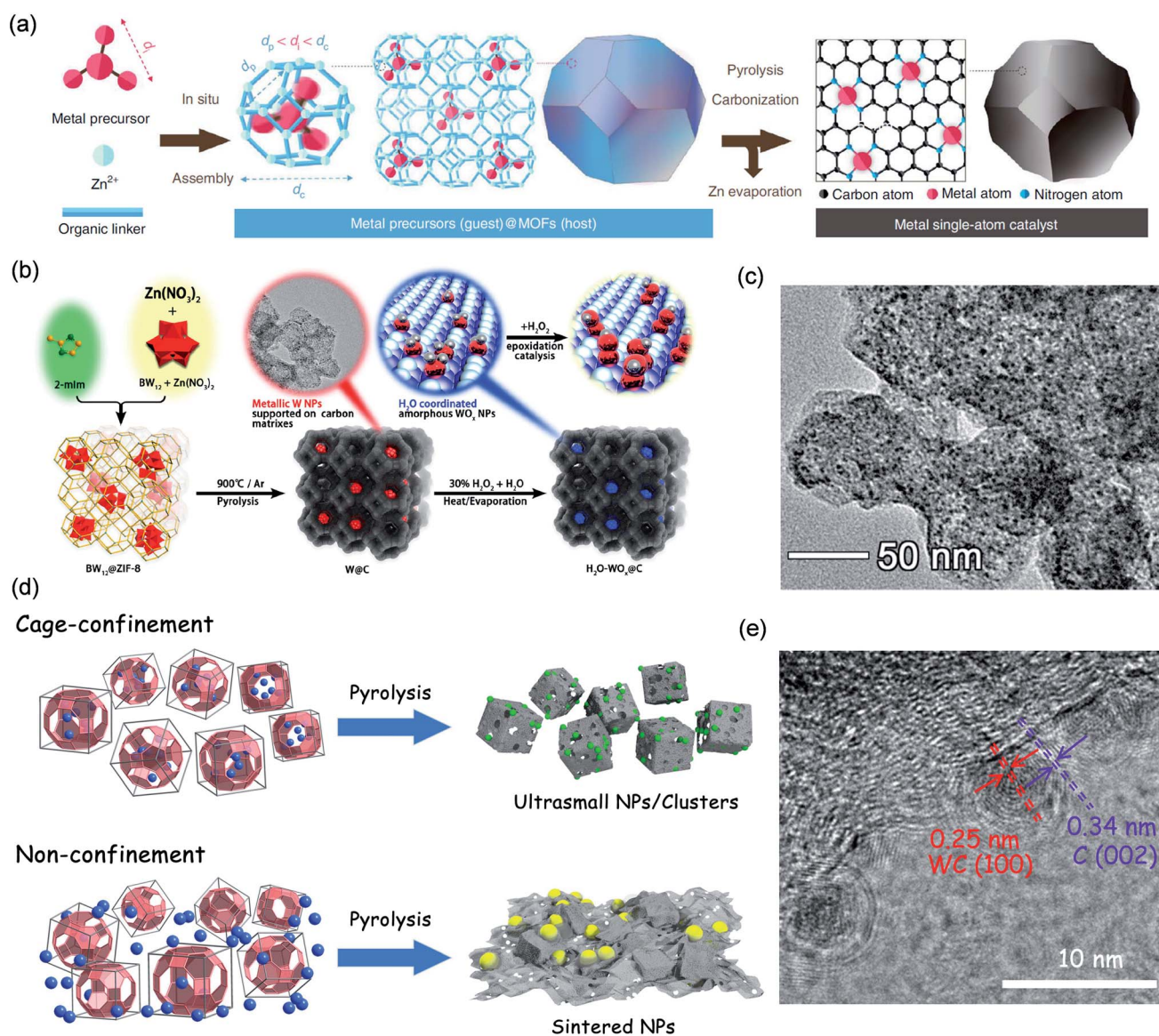


Fig. 13 Cases of space-confinement pyrolysis. (a) Schematic illustration of constructing  $M_1/CN$ . Reproduced with permission.<sup>139</sup> Copyright 2020, Springer Nature. Construction schematic and TEM images of (b and c)  $H_2O-WO_x@C$ . Reproduced with permission.<sup>141</sup> Copyright 2019, American Chemical Society. and (d and e)  $WC@NPC$ . Reproduced with permission.<sup>142</sup> Copyright 2017, American Chemical Society.



value of Ru<sub>3</sub>/CN was superior to that of ultrafine Ru NPs (*ca.* 2.5 nm).

POMs have an adjustable molecular size, clear structure, and good solubility, making them ideal catalyst precursors. Niu *et al.* used molecular cages in MAF-4 to encapsulate Keggin-type K<sub>5</sub>BW<sub>12</sub>O<sub>40</sub> (BW<sub>12</sub>), followed by pyrolysis and oxidation, to synthesize ultrafine H<sub>2</sub>O-WO<sub>x</sub> NPs (H<sub>2</sub>O-WO<sub>x</sub>@C) for the olefin epoxidation reaction (Fig. 13b).<sup>141</sup> MAF-4 and BW<sub>12</sub> were selected as the host and guest molecules due to the following reasons. Firstly, the size of a single BW<sub>12</sub> anion is 0.9 nm, which is smaller than the cage size of MAF-4 (1.16 nm) and larger than the cage window size (0.34 nm), so it can be encapsulated in the cage without being leached from its window. Secondly, BW<sub>12</sub> is very stable in the process of *in situ* packaging to form BW<sub>12</sub>@MAF-4. Thirdly, the K<sup>+</sup> ions that compete with BW<sub>12</sub> anions and can be located in adjacent molecular cages encapsulating BW<sub>12</sub>, which can ensure that BW<sub>12</sub> was evenly distributed in MAF-4. Thanks to the space-confinement of the hybrid cages, the migration and agglomeration of metal precursors could be effectively reduced, thus preparing ultrafine W NPs. The average size of the highly dispersed ultrafine W NPs in the as-synthesized W@C was 2.28 nm (Fig. 13c). After oxidation, H<sub>2</sub>O-WO<sub>x</sub> still maintained the ultrafine nanoparticle structure with highly uniform dispersion. The final H<sub>2</sub>O-WO<sub>x</sub>@C showed high catalytic activity for the epoxidation of olefins with high conversion (98.6%) and selectivity (99%).

Compared with MAF-4, MAF-6 possesses a larger nanocage with a diameter of *ca.* 1.84 nm, a highly hydrophobic pore surface, a flexible small pore window (average diameter = 0.76 nm), and good thermal/chemical stability, which is also chosen as the host for even larger guest molecules (*e.g.* metal carbonyl compounds) to confine the construction of ultrafine MNPs.<sup>142</sup>

For example, we have reported the synthesis of ultrafine WC nanoclusters by using the HSCP method based on MAF-6 (Fig. 13d).<sup>142</sup> The guest molecule W(CO)<sub>6</sub> (molecular diameter of *ca.* 0.92 nm) could be encapsulated and isolated in the nanocavity of MAF-6 without leaching out of its window through low temperature vapor adsorption. Subsequently, WC@NPC was constructed by pyrolyzing the W(CO)<sub>6</sub>@MAF-6 precursor. The ultrafine WC NPs (*ca.* 2.0 nm) were highly dispersed and uniformly embedded in the carbon substrate (Fig. 13e). For comparison, a mechanically mixed precursor of W(CO)<sub>6</sub>/MAF-6 was constructed by adding W(CO)<sub>6</sub> directly during the preparation of MAF-6, and in the same pyrolysis process, only W NPs could be obtained with obvious agglomeration that resulted in uneven sizes of 5–55 nm. The carbon protected WC nanoclusters showed excellent hydrogen evolution reaction activity and durability. In 0.5 M H<sub>2</sub>SO<sub>4</sub>, the overpotential for WC@NPC at 10 mA cm<sup>-2</sup> was 51 mV with a small Tafel slope of 49 mV per decade. WC@NPC presented an extremely high exchange current density (2.4 mA cm<sup>-2</sup>), surpassing all tungsten/molybdenum-based electrocatalysts reported in advance. The different distribution of W(CO)<sub>6</sub> molecules in MAF-6 and the confinement effect of the porous framework may determine the huge difference between the resultant MNPs, not just the particle sizes but even the crystalline phases.

**4.1.2. Organic space-confinement pyrolysis.** COFs or POPs have a wealth of nanopores constructed from pure organic species with adjustable sizes. It is easy to achieve precise control of nanopores as well as pore surfaces by changing the types of organic monomers. These organic nanopores can isolate metal precursors and effectively reduce their migration and agglomeration during the pyrolysis process, thereby resulting in ultrafine MNPs.<sup>143</sup> In addition, COFs or POPs also have excellent structural robustness, existing stably in various solvent systems to meet the requirements for uniformly encapsulating metal precursors into their nanopores.

Li *et al.* synthesized a metal isolated single-atom site (ISAS) catalyst (M-ISAS/p-CN) supported on porous nitrogen-doped carbon using the OSCP method.<sup>144</sup> Firstly, Co(acac)<sub>2</sub>@PDA nanospheres were prepared by *in situ* encapsulation of cobalt acetylacetonate during the polymerization of dopamine monomers. Subsequently, Co-ISAS/p-CN was constructed *via* controlling the pyrolysis of the Co(acac)<sub>2</sub>@PDA precursor. This strategy had broad applicability and was suitable for the preparation of a variety of M-ISAS/p-CN (*e.g.* M = Cu, Co, Ni, Pd, Mn) catalysts, which still maintained the uniform nano-spherical appearance. Taking Co-ISAS/p-CN as an example, the EXAFS spectrum confirmed that there were no Co–Co chemical bonds, indicating that Co was dispersed in p-CN in the form of single-atom sites. In addition, a series of characterization techniques confirmed that the Co single atom existed in the form of coordination with four N atoms. Co-ISAS/p-CN showed excellent electrochemical ORR activity with a half-wave potential of 0.838 V.

Huang *et al.* also used the OSCP strategy for preparing ultrafine Mo<sub>2</sub>C NPs.<sup>145</sup> Firstly, PMo<sub>12</sub>@PPy/CNT was constructed through polymerization, crosslinking and coating between CNTs, pyrrole, 5,10,15,20-tetrakis(4-carboxyphenyl) porphyrin (TCPP) and PMo<sub>12</sub> molecules. In the process of pyrrole polymerizing around the outer layer of CNTs to form a polymer chain, the 4 carboxyl groups on the TCPP molecule and the N–H group on the PPy were cross-linked by 4 hydrogen bonds, resulting in nanopores with a diameter of ~1.8 nm. The diameter of PMo<sub>12</sub> is about 1.05 nm, so one nanopore can hold exactly one PMo<sub>12</sub> molecule. Subsequently, size-controllable Mo<sub>2</sub>C NPs (Mo<sub>2</sub>C@NPC/CNT) coated with N and P co-doped carbon shells were prepared by pyrolyzing PMo<sub>12</sub>@PPy/CNT. The uniform embedding of Mo<sub>2</sub>C NPs in the carbon matrix during carbonization was due to the perfect confinement of these molecule-scale organic cages. The optimized Mo<sub>2</sub>C NPs were only 5.0 nm and were wrapped by 2–4 layers of ultrathin carbon and uniformly dispersed in Mo<sub>2</sub>C@NPC/CNT. Mo<sub>2</sub>C@NPC/CNT exhibited good electrochemical performance for the electrochemical sensing of acetaminophen (AC) and dopamine (DA) simultaneously, showing detection limits (S/N = 3) of 0.01 and 0.008 μM for DA and AC.

## 4.2. Coordination-confinement pyrolysis

The CCP strategy is the use of coordinated interactions between the coordinating atoms on PMMs and targeted metal ions to achieve confinement. Many PMMs are rich in coordination



atoms (such as O, N, S, P, *etc.*), which can bind various metal ions to form monodisperse metal centers with appropriate distances, thus effectively reducing the diffusion and agglomeration of metals during the pyrolysis process.<sup>146–151</sup> The coordination heteroatoms can be doped *in situ* on the carbon substrate formed by carbonization to modulate the electronic structures of MNPs or single atom sites and can also induce the metal precursors to form various functional metal compounds at high temperature, such as metal sulfides, metal phosphides, metal nitrides, *etc.*, which are very difficult to make into ultra-fine sizes by conventional methods.<sup>152–159</sup>

Wu *et al.* reported an organic ligand CCP method to synthesize a Co single-atom catalyst and regulated the electrocatalytic CO<sub>2</sub> reduction performance of the catalyst by adjusting the coordination number of a single Co site (Fig. 14a).<sup>160</sup> Thanks to the coordination confinement effect of the N atoms on the ligands, the transport and accumulation of Co were significantly reduced to obtain a Co single-atom catalyst. The coordination number of Co (Co–N<sub>4</sub>, Co–N<sub>3</sub>, and Co–N<sub>2</sub>) could be regulated by the pyrolysis temperature, and the higher the temperature, the lower the coordination number. Co–N<sub>2</sub> exhibited the best electrocatalytic CO<sub>2</sub>RR activity and selectivity, the CO Faraday efficiency was as high as 94%, and the TOF value

was up to 18 200 h<sup>–1</sup>. Experiments and theoretical calculations confirmed that a lower coordination number was beneficial to the activation of CO<sub>2</sub> to the CO<sub>2</sub><sup>–</sup> intermediate, which in turn promoted the CO<sub>2</sub> reduction activity of the catalyst.

Jiang *et al.* used a porphyrinic MOF to coordinate Fe<sup>3+</sup> for synthesizing Fe single atoms (Fig. 14b).<sup>161</sup> Fe<sub>x</sub>-PCN-222, being isomorphous to PCN-222, was constructed by the self-assembly of Fe-TCPP (TCPP = tetrakis-(4-carboxyphenyl)porphyrin), H<sub>2</sub>-TCPP and ZrOCl<sub>2</sub> · 8H<sub>2</sub>O. By controlling the ratio of Fe-TCPP and H<sub>2</sub>-TCPP, the distance between Fe-TCPP units in adjacent Fe<sub>x</sub>-PCN-222 could be optimized. The optimized Fe<sub>20</sub>-PCN-222 was converted into Fe single atoms (FeSA-N-C) implanted in porous nitrogen-doped carbon after pyrolysis and subsequent removal of ZrO<sub>2</sub>. EXAFS fitting confirmed that each Fe atom formed a four-coordinate structure with nitrogen. The formation of single-atom Fe was attributed to the coordination-confinement effect of four N, which could anchor Fe, and then directly retained in the final structure by high temperature pyrolysis. The ORR activity of FeSA-N-C (*E*<sub>1/2</sub> = 0.891 V) was better than that of commercial Pt/C (*E*<sub>1/2</sub> = 0.848 V).

In addition to organic ligand CCP, MOFs can also achieve metal node CCP. Zhang *et al.* used the confinement effect of metal nodes in UiO-66 to synthesize atomic-level Ir sites

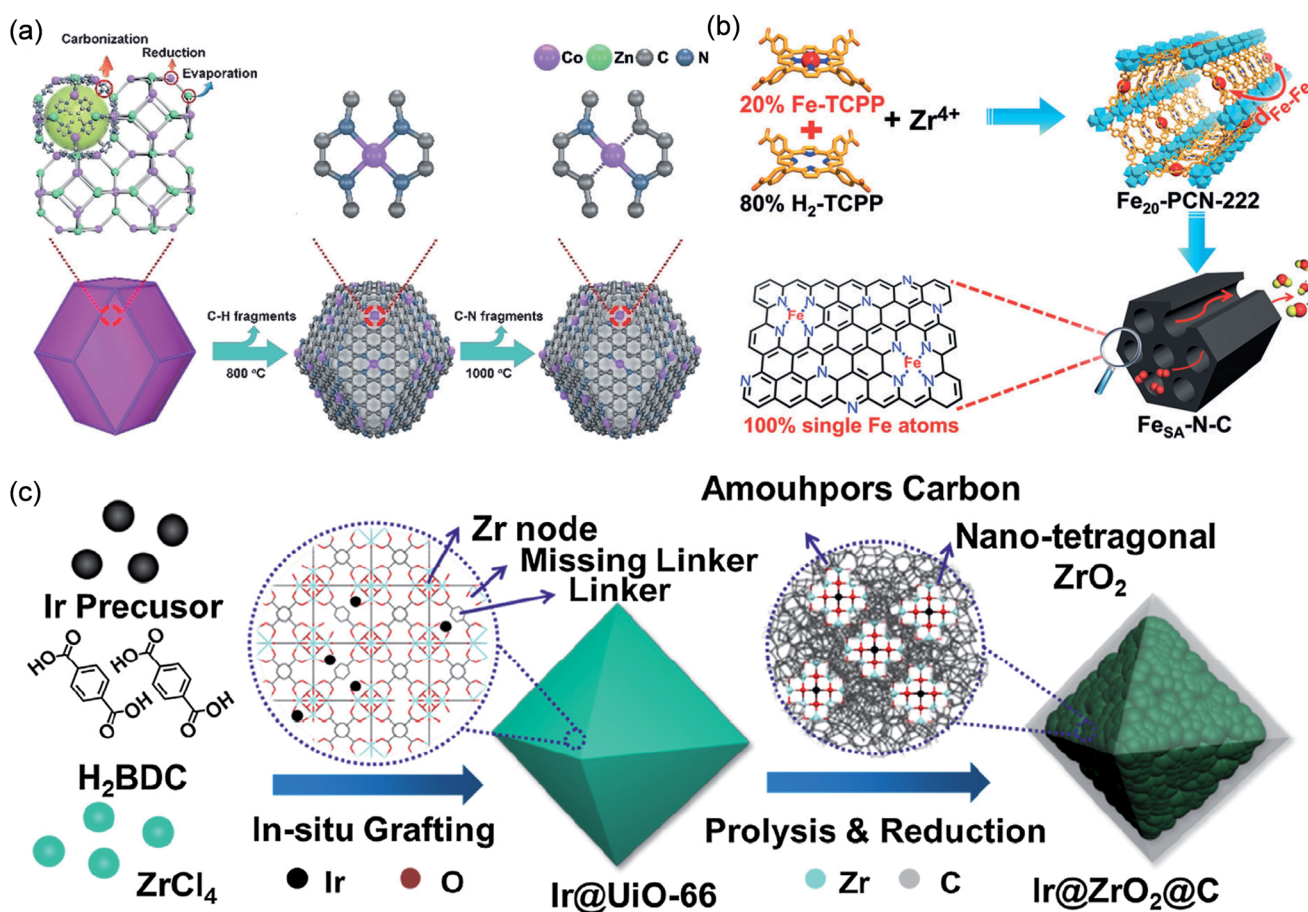


Fig. 14 Cases of MOF coordination-confinement pyrolysis. Schematic illustration of constructing (a) Co–N<sub>4</sub>, Co–N<sub>3</sub>, and Co–N<sub>2</sub>. Reproduced with permission.<sup>160</sup> Copyright 2018, WILEY-VCH. (b) FeSA-N-C. Reproduced with permission.<sup>161</sup> Copyright 2018, WILEY-VCH. (c) Ir@ZrO<sub>2</sub>@C. Reproduced with permission.<sup>162</sup> Copyright 2019, Elsevier.



(Fig. 14c).<sup>162</sup> The metal node  $Zr_6$  in UiO-66 is rich in hydroxyl groups, which can chelate metal ions. Firstly,  $Ir@UiO-66$  was prepared by *in situ* grafting an Ir precursor during MOF synthesis. Subsequently,  $Ir@ZrO_2@C$  was constructed by pyrolysis of  $Ir@UiO-66$  to obtain  $Ir@ZrO_2@C$ , which maintained well the octahedral morphology. A large number of  $ZrO_2$  NPs (*ca.* 3.0 nm) were formed in  $Ir@ZrO_2@C$ , but no Ir NPs were found. In the PXRD pattern of  $Ir@ZrO_2@C$ , there was only the diffraction peak of  $ZrO_2$  but no diffraction peak of Ir elementary substance, indicating the possible presence of monodisperse Ir. The formation of atomic-level Ir sites was attributed to the strong coordination of  $-OH$  to Ir on the Zr node in UiO-66, which made it difficult for Ir to migrate and aggregate during the pyrolysis process.  $Ir@ZrO_2@C$  was a good acid-resistant catalyst, showing great conversion efficiency in the hydrogenation reaction of levulinic acid to  $\gamma$ -valerolactone. The high performance was attributed to the enhanced synergy between the atomically dispersed Ir species and the  $ZrO_2$  carrier, as well as the protective effect of the *in situ* derived amorphous carbon.

COFs can also achieve organic CCP for synthesizing ultrafine MNPs.<sup>163–165</sup> Li *et al.* used a COF-absorption-pyrolysis approach for preparing various isolated single atom site (ISAS) catalysts (Fig. 15a).<sup>166</sup> Firstly, RT-COF-1 was constructed through the condensation reaction of organic monomers 1,3,5-tris(4-aminophenyl) benzene and 1,3,5-benzenetricarboxaldehyde. Then, the metal ions were uniformly anchored in RT-COF-1 using the coordination effect of the N atoms. Finally, the RT-COF-1 precursor with metal ions was pyrolyzed to construct ISAS catalysts (M-ISAS/CN, M = Fe, Co, Ni) embedded in

a carbon substrate. M-ISAS/CN still maintained the morphology of RT-COF-1 precursor nanospheres, and no MNPs were found to be formed. Fe-ISAS/CN was taken as an example. FT-EXAFS revealed the existence of Fe–N/C bonds in Fe-ISAS/CN but no Fe–Fe bonds, indicating that Fe existed as a SA. Fe-ISAS/CN displayed good ORR activity with a kinetic current density as high as  $5.47 \text{ mA cm}^{-2}$  at 0.85 V. In addition, Fe-ISAS/CN exhibited good stability and methanol tolerance.

Zhang *et al.* utilized a polymer-assisted pyrolysis strategy to construct a Co SAC and proved that the incorporated P can coordinate with Co to improve its ORR activity.<sup>167</sup> The poly(HCCP-TA-BPS) (HCCP = hexachlorocyclotriphosphazene, TA = tannic acid, BPS = 4,4'-sulfonyldiphenol) nanospheres (PSTA) have a large number of catechol groups, which can chelate  $Co^{2+}$  ions to obtain PSTA-Co. Finally, PSTA-Co was pyrolyzed to prepare  $Co-N_2P_2$  monoatomic sites uniformly dispersed in PSTA-Co-1000. Due to the chelation between the coordination atom and  $Co^{2+}$ , the agglomeration of metals during the pyrolysis process could be reduced to prepare atomic-scale Co sites. EXAFS confirmed the existence of Co–N and Co–P in PSTA-Co-1000, but no Co–Co, indicating that a single Co atom was formed in the catalyst. EXAFS fitting revealed that the average coordination numbers of Co with N and P were 2.1 and 1.9, respectively. PSTA-Co-1000 exhibited good electrocatalytic ORR activity with a half-wave potential of 0.878 V. Compared with  $Co-N_4$ , theoretical calculations showed that the  $Co-N_2P_2$  active center could be more effectively combined with oxygen to drive the ORR, with faster ORR kinetics.

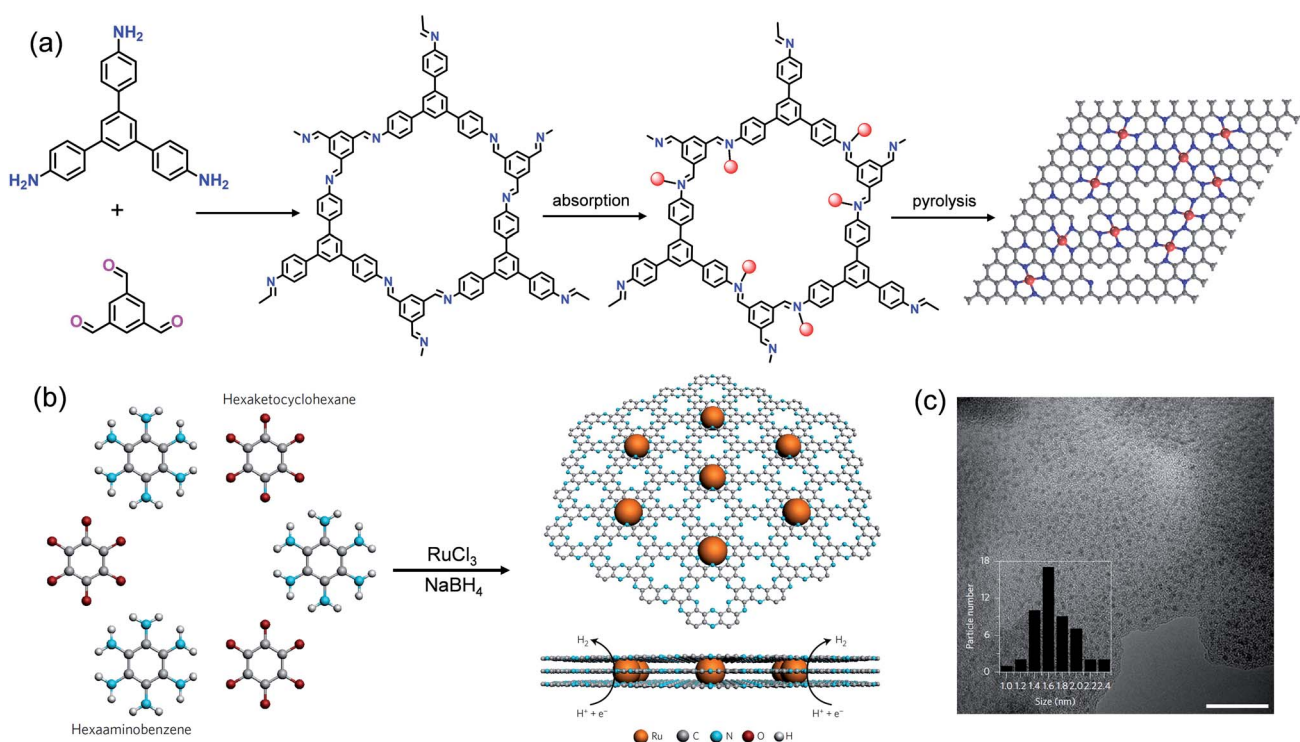


Fig. 15 Cases of COF or POP coordination-confinement pyrolysis. Schematic illustration of constructing (a) Fe-ISAS/CN and (b)  $Ru@C_2N$ . (c) TEM image of  $Ru@C_2N$ . Reproduced with permission.<sup>168</sup> Copyright 2017, Springer Nature.



Baek *et al.* constructed a N-rich porous polymer (C<sub>2</sub>N) using the polycondensation reaction of organic monomers hexaketocyclohexane (HKH) and hexaaminobenzene (HAB) trihydrochloride, and synthesized Ru NPs (Ru@C<sub>2</sub>N) with the coordination-confinement of Ru<sup>3+</sup> ions and subsequent pyrolysis (Fig. 15b).<sup>168</sup> The BET surface area of Ru@C<sub>2</sub>N reached 400.1 m<sup>2</sup> g<sup>-1</sup>. TEM showed that the ultrafine Ru NPs with a diameter of *ca.* 1.6 nm were uniformly distributed in the C<sub>2</sub>N supports (Fig. 15c). The formation of ultrafine nanostructures was attributed to the high density N sites in C<sub>2</sub>N, which could provide nucleation sites for Ru atoms and limit their migration and aggregation. The resultant Ru@C<sub>2</sub>N exhibited excellent HER activity and stability. The overpotentials for Ru@C<sub>2</sub>N at 10 mA cm<sup>-2</sup> were only 17.0 (1.0 M KOH) and 13.5 mV (0.5 M H<sub>2</sub>SO<sub>4</sub>), surpassing commercial Pt/C and better than most reported catalysts.

## 5. Conclusions and prospects

This review article introduced the latest progress on the confinement synthesis in PMMs for synthesizing atomic-scale nanostructures. PMMs show superb advantages in constituent modulation and structural modification. The building blocks, organic functional groups, or metal nodes in PMMs can be accurately regulated at the atomic level. Therefore, it is possible to design and construct adjustable nano/sub-nano-confined spaces and modify various types of coordinated heteroatoms in PMMs. PMMs exhibit unique advantages of space-confinement, coordination-confinement, and ion-confinement, which can not only significantly reduce the agglomeration of MNPs, but also limit the growth of MNPs to obtain well-dispersed ultrafine MNPs. Additionally, PMMs can serve as desired templates or precursors to derive various ultrafine nanostructures benefiting from their special molecular construction and confinement effects. The abundant nanocages/pores and coordination atoms in PMMs can isolate and anchor metal precursors/metal ions to limit the atom diffusion and aggregation during the pyrolysis process. Moreover, PMMs can easily form hybrid carbon layers at high temperature, which not only regulate the electron structures of the atom-dispersed metal nanomaterials but also protect them from agglomeration or degradation in harsh chemical environments. By using these strategies, new multifunctional and highly active materials based on PMMs or their derivatives will appear in the future.

Despite the tremendous successes, PMM-confinement research still faces some challenges. Firstly, most confinement strategies currently focus on the synthesis of ultrafine precious MNPs, like Au, Pt, Ru, *etc.* There are few reports on the construction of ultrafine non-noble MNPs by the PMM-confinement strategy, because non-precious MNPs present higher surface energy and more reactivity under oxidation and reduction conditions, tending to aggregate and become larger. Actually, easy-to-obtain and non-expensive MNPs have broader application prospects. Therefore, it is necessary to propose an effective PMM-confinement strategy to synthesize ultrafine yet stable non-noble MNPs. Secondly, the PMM-confinement strategy is mostly applied to the construction of metals or

their alloys. The synthesis of ultrafine and stable metal phosphides, nitrides, and chalcogenides is rarely achieved, and these ultrafine nanostructures often show superior activity in heterocatalysis, especially the catalytic conversions of small energy molecules. Applying the PMM-confinement strategy to synthesize a richer variety of ultrafine nanostructures can make it more universal and expand its application fields. Thirdly, it is necessary to develop multi-confinement combination strategies, such as space-ion-confinement, space-coordination-confinement and so on, which may provide the possibility for the synthesis of more types of ultrafine nanostructures, such as multi-component ultrafine nanocrystals, single atom loaded nanoclusters, diatomic or triatomic site catalysts, *etc.* Moreover, it is also important to study the influence of different pore sizes and pore surface characteristics in PMMs, such as hydrophilicity and hydrophobicity, on the confinement synthesis of MNPs, as well as the influence of different functional groups or coordination on their morphologies and sizes, which would guide the rational design and construction of ideal PMMs for the confinement synthesis of specifically functional MNPs. Furthermore, the development of more widely sourced, lower cost PMM materials, such as biomass macromolecules, as domain-confinement templates is also desirable, which is conducive to the large-scale preparation of highly active ultrafine nanomaterials.

## Author contributions

C.-T. H. conceived the concept and supervised the project. L.-M. Cao and J. Z. collected references, organized images and wrote the initial manuscript. X.-F. Z. modified the images and participated in discussions. All the authors discussed the results, revised and commented on the manuscript.

## Conflicts of interest

There are no conflicts to declare.

## Acknowledgements

This work was supported by the National Natural Science Foundation of China (21901088, 21901089, 32101750 and 22161021) and the Natural Science Foundation of Jiangxi Province (20212BAB203021 and 20202ZDB01004). C.-T. He acknowledges the support of Jiangxi Province (jxsq2018106041) and the “Young Elite Scientists Sponsorship Program” by CAST.

## Notes and references

- 1 L. C. Liu and A. Corma, *Chem. Rev.*, 2018, **118**, 4981–5079.
- 2 L. L. Zhang, M. X. Zhou, A. Q. Wang and T. Zhang, *Chem. Rev.*, 2020, **120**, 683–733.
- 3 Z. Li, S. F. Ji, Y. W. Liu, X. Cao, S. B. Tian, Y. J. Chen, Z. G. Niu and Y. D. Li, *Chem. Rev.*, 2020, **120**, 623–682.
- 4 L. He, F. Weniger, H. Neumann and M. Beller, *Angew. Chem., Int. Ed.*, 2016, **55**, 12582–12594.



- 5 I. F. Teixeira, E. C. M. Barbosa, S. C. E. Tsang and P. H. C. Camargo, *Chem. Soc. Rev.*, 2018, **47**, 7783–7817.
- 6 H. Tabassum, A. Mahmood, B. J. Zhu, Z. B. Liang, R. Q. Zhong, S. J. Guo and R. Q. Zou, *Energy Environ. Sci.*, 2019, **12**, 2924–2956.
- 7 C. B. Gao, F. L. Lyu and Y. D. Yin, *Chem. Rev.*, 2021, **121**, 834–881.
- 8 G. Palumbo, S. J. Thorpe and K. T. Aust, *Nanocryst. Mater.*, 1990, **24**, 1347–1350.
- 9 J. N. Kuhn, W. Y. Huang, C. K. Tsung, Y. W. Zhang and G. A. Somorjai, *J. Am. Chem. Soc.*, 2008, **130**, 14026–14027.
- 10 B. Xiao, Z. Q. Niu, Y. G. Wang, W. Jia, J. Shang, L. Zhang, D. S. Wang, Y. Fu, J. Zeng, W. He, K. Wu, J. Li, J. L. Yang, L. Liu and Y. D. Li, *J. Am. Chem. Soc.*, 2015, **137**, 3791–3794.
- 11 M. L. Ding, R. W. Flaig, H. L. Jiang and O. M. Yaghi, *Chem. Soc. Rev.*, 2019, **48**, 2783–2828.
- 12 M. T. Zhao, K. Yuan, Y. Wang, G. D. Li, J. Guo, L. Gu, W. P. Hu, H. J. Zhao and Z. Y. Tang, *Nature*, 2016, **539**, 76–80.
- 13 C. T. He, L. Jiang, Z. M. Ye, R. Krishna, Z. S. Zhong, P. Q. Liao, J. Q. Xu, G. F. Ouyang, J. P. Zhang and X. M. Chen, *J. Am. Chem. Soc.*, 2015, **137**, 7217–7223.
- 14 L. Y. Chen, R. Luque and Y. W. Li, *Chem. Soc. Rev.*, 2017, **46**, 4614–4630.
- 15 M. T. Zhao, Y. Huang, Y. W. Peng, Z. Q. Huang, Q. L. Ma and H. Zhang, *Chem. Soc. Rev.*, 2018, **47**, 6267–6295.
- 16 D. P. Halter, R. A. Klein, M. A. Boreen, B. A. Trump, C. M. Brown and J. R. Long, *Chem. Sci.*, 2020, **11**, 6709–6716.
- 17 C. R. Marshall, S. A. Staudhammer and C. K. Brozek, *Chem. Sci.*, 2019, **10**, 9396–9408.
- 18 Z. W. Fu, X. Y. Wang, A. Gardner, X. Wang, S. Y. Chong, G. Neri, A. J. Cowan, L. J. Liu, X. B. Li, A. Vogel, R. Clowes, M. Bilton, L. J. Chen, R. S. Sprick and A. I. Cooper, *Chem. Sci.*, 2020, **11**, 543–550.
- 19 F. Beuerle and B. Gole, *Angew. Chem., Int. Ed.*, 2018, **57**, 4850–4878.
- 20 J. L. Segura, S. Royuela and M. M. Ramos, *Chem. Soc. Rev.*, 2019, **48**, 3903–3945.
- 21 X. Y. Guan, F. Q. Chen, Q. R. Fang and S. L. Qiu, *Chem. Soc. Rev.*, 2020, **49**, 1357–1384.
- 22 Z. F. Wang, S. N. Zhang, Y. Chen, Z. J. Zhang and S. Q. Ma, *Chem. Soc. Rev.*, 2020, **49**, 708–735.
- 23 X. Kang, X. W. Wu, X. Han, C. Yuan, Y. Liu and Y. Cui, *Chem. Sci.*, 2020, **11**, 1494–1502.
- 24 G. D. Li, S. L. Zhao, Y. Zhang and Z. Y. Tang, *Adv. Mater.*, 2018, **30**, 1800702.
- 25 Q. H. Yang, Q. Xu and H. L. Jiang, *Chem. Soc. Rev.*, 2017, **46**, 4774–4808.
- 26 R. Tao, X. R. Ma, X. L. Wei, Y. H. Jin, L. Qiu and W. Zhang, *J. Mater. Chem. A*, 2020, **8**, 17360–17391.
- 27 J. Y. Kim, H. Oh and H. R. Moon, *Adv. Mater.*, 2019, **31**, 1805293.
- 28 N. Wang, Q. M. Sun and J. H. Yu, *Adv. Mater.*, 2019, **31**, 1803966.
- 29 H. Y. Hu, S. L. Lu, T. Li, Y. Zhang, C. X. Guo, H. Zhu, Y. H. Jin, M. L. Du and W. Zhang, *Nanoscale Adv.*, 2021, **3**, 1865–1886.
- 30 Q. L. Zhu and Q. Xu, *Chem*, 2016, **1**, 220–245.
- 31 L. Y. Chen, H. F. Wang, C. X. Li and Q. Xu, *Chem. Sci.*, 2020, **11**, 5369–5403.
- 32 P. Y. Ju, S. J. Wu, Q. Su, X. D. Li, Z. Q. Liu, G. H. Li and Q. L. Wu, *J. Mater. Chem. A*, 2019, **7**, 2660–2666.
- 33 H. C. Ma, J. L. Kan, G. J. Chen, C. X. Chen and Y. B. Dong, *Chem. Mater.*, 2017, **29**, 6518–6524.
- 34 X. L. Li, T. W. Goh, L. Li, C. X. Xiao, Z. Y. Guo, X. C. Zeng and W. Y. Huang, *ACS Catal.*, 2016, **6**, 3461–3468.
- 35 H. Zhao, G. Q. Yu, M. Yuan, J. Yang, D. Xu and Z. P. Dong, *Nanoscale*, 2018, **10**, 21466–21474.
- 36 A. Aijaz, A. Karkamkar, Y. J. Choi, N. Tsumori, E. Ronnebro, T. Autrey, H. Shioyama and Q. Xu, *J. Am. Chem. Soc.*, 2012, **134**, 13926–13929.
- 37 Q. L. Zhu, J. Li and Q. Xu, *J. Am. Chem. Soc.*, 2013, **135**, 10210–10213.
- 38 M. Y. Fan, W. D. Wang, Y. Y. Zhu, X. Sun, F. W. Zhang and Z. P. Dong, *Appl. Catal., B*, 2019, **257**, 117942.
- 39 S. Hermes, M. K. Schroter, R. Schmid, L. Khodeir, M. Muhler, A. Tissler, R. W. Fischer and R. A. Fischer, *Angew. Chem., Int. Ed.*, 2005, **44**, 6237–6241.
- 40 J. Hermannsdorfer, M. Friedrich, N. Miyajima, R. Q. Albuquerque, S. Kummel and R. Kempe, *Angew. Chem., Int. Ed.*, 2012, **51**, 11473–11477.
- 41 Y. W. Liu, X. Wu, Z. Li, J. Zhang, S. X. Liu, S. J. Liu, L. Gu, L. R. Zheng, J. Li, D. S. Wang and Y. D. Li, *Nat. Commun.*, 2021, **12**, 4205.
- 42 X. H. Liu, J. G. Ma, Z. Niu, G. M. Yang and P. Cheng, *Angew. Chem., Int. Ed.*, 2015, **54**, 988–991.
- 43 F. Schroeder, D. Esken, M. Cokoja, M. W. E. van den Berg, O. I. Lebedev, G. van Tendeloo, B. Walaszek, G. Buntkowsky, H. H. Limbach, B. Chaudret and R. A. Fischer, *J. Am. Chem. Soc.*, 2008, **130**, 6119–6130.
- 44 J. Hermannsdorfer and R. Kempe, *Chem.–Eur. J.*, 2011, **17**, 8071–8077.
- 45 Y. Y. Pan, B. Z. Yuan, Y. W. Li and D. H. He, *Chem. Commun.*, 2010, **46**, 2280–2282.
- 46 Y. B. Huang, Z. J. Lin and R. Cao, *Chem.–Eur. J.*, 2011, **17**, 12706–12712.
- 47 B. Z. Yuan, Y. Y. Pan, Y. W. Li, B. L. Yin and H. F. Jiang, *Angew. Chem., Int. Ed.*, 2010, **49**, 4054–4058.
- 48 M. S. El-Shall, V. Abdelsayed, A. E. R. S. Khder, H. M. A. Hassan, H. M. El-Kaderi and T. E. Reich, *J. Mater. Chem.*, 2009, **19**, 7625–7631.
- 49 Y. B. Huang, T. Ma, P. Huang, D. S. Wu, Z. J. Lin and R. Cao, *ChemCatChem*, 2013, **5**, 1877–1883.
- 50 X. M. Zhao, Y. Jin, F. M. Zhang, Y. J. Zhong and W. D. Zhu, *Chem. Eng. J.*, 2014, **239**, 33–41.
- 51 H. L. Liu, Y. W. Li, R. Luque and H. F. Jiang, *Adv. Synth. Catal.*, 2011, **353**, 3107–3113.
- 52 Y. Z. Chen, Q. Xu, S. H. Yu and H. L. Jiang, *Small*, 2015, **11**, 71–76.
- 53 M. Yadav and Q. Xu, *Chem. Commun.*, 2013, **49**, 3327–3329.
- 54 J. Hermannsdorfer, M. Friedrich and R. Kempe, *Chem.–Eur. J.*, 2013, **19**, 13652–13657.



- 55 C. Zlotea, R. Campesi, F. Cuevas, E. Leroy, P. Dibandjo, C. Volkringer, T. Loiseau, G. Ferey and M. Latroche, *J. Am. Chem. Soc.*, 2010, **132**, 2991–2997.
- 56 Y. A. Li, S. Yang, Q. K. Liu, G. J. Chen, J. P. Ma and Y. B. Dong, *Chem. Commun.*, 2016, **52**, 6517–6520.
- 57 Y. W. Liu, B. X. Wang, Q. Fu, W. Liu, Y. Wang, L. Gu, D. S. Wang and Y. D. Li, *Angew. Chem., Int. Ed.*, 2021, **60**, 22522–22528.
- 58 X. W. Lan, C. Du, L. L. Cao, T. T. She, Y. M. Li and G. Y. Bai, *ACS Appl. Mater. Interfaces*, 2018, **10**, 38953–38962.
- 59 R. Khatun, S. Biswas, I. H. Biswas, S. Riyajuddin, N. Haque, K. Ghosh and S. M. Islam, *J. CO<sub>2</sub> Util.*, 2020, **40**, 101180.
- 60 L. P. Zhai, S. Yang, X. B. Yang, W. Y. Ye, J. Wang, W. H. Chen, Y. Guo, L. W. Mi, Z. J. Wu, C. Soutis, Q. Xu and Z. Jiang, *Chem. Mater.*, 2020, **32**, 9747–9752.
- 61 H. C. Ma, C. C. Zhao, G. J. Chen and Y. B. Dong, *Nat. Commun.*, 2019, **10**, 3368.
- 62 Q. Zhuang, R. R. Gao, M. Y. Shi, X. P. Lin, A. M. Xie and W. Dong, *ACS Appl. Nano Mater.*, 2021, **4**, 3869–3876.
- 63 W. Gong, Q. Q. Wu, G. X. Jiang and G. J. Li, *J. Mater. Chem. A*, 2019, **7**, 13449–13454.
- 64 J. K. Sun, W. W. Zhan, T. Akita and Q. Xu, *J. Am. Chem. Soc.*, 2015, **137**, 7063–7066.
- 65 Y. Zhang, Y. Xiong, J. Ge, R. Lin, C. Chen, Q. Peng, D. S. Wang and Y. D. Li, *Chem. Commun.*, 2018, **54**, 2796–2799.
- 66 R. McCaffrey, H. Long, Y. H. Jin, A. Sanders, W. Park and W. Zhang, *J. Am. Chem. Soc.*, 2014, **136**, 1782–1785.
- 67 L. Qiu, R. McCaffrey, Y. H. Jin, Y. Gong, Y. M. Hu, H. L. Sun, W. Park and W. Zhang, *Chem. Sci.*, 2018, **9**, 676–680.
- 68 B. Mondal, K. Acharyya, P. Howlader and P. S. Mukherjee, *J. Am. Chem. Soc.*, 2016, **138**, 1709–1716.
- 69 G. J. Chen, W. L. Xin, J. S. Wang, J. Y. Cheng and Y. B. Dong, *Chem. Commun.*, 2019, **55**, 3586–3589.
- 70 K. Suzuki, S. Sato and M. Fujita, *Nat. Chem.*, 2010, **2**, 25–29.
- 71 J. Yang, M. Yuan, D. Xu, H. Zhao, Y. Y. Zhu, M. Y. Fan, F. W. Zhang and Z. P. Dong, *J. Mater. Chem. A*, 2018, **6**, 18242–18251.
- 72 W. Zhao, Y. Z. Jiao, J. J. Li, L. P. Wu, A. Xie and W. Dong, *J. Catal.*, 2019, **378**, 42–50.
- 73 X. C. Yang, J. K. Sun, M. Kitta, H. Pang and Q. Xu, *Nat. Catal.*, 2018, **1**, 214–220.
- 74 L. Y. Chen, H. R. Chen, R. Luque and Y. W. Li, *Chem. Sci.*, 2014, **5**, 3708–3714.
- 75 Z. M. Cui, T. Fan, L. Y. Chen, R. Q. Fang, C. M. Li and Y. W. Li, *Sci. China: Chem.*, 2021, **64**, 109–115.
- 76 M. Martis, K. Mori, K. Fujiwara, W. S. Ahn and H. Yamashita, *J. Phys. Chem. C*, 2013, **117**, 22805–22810.
- 77 Y. L. Jiang, Y. Yu, X. Zhang, M. Weinert, X. L. Song, J. Ai, L. Han and H. H. Fei, *Angew. Chem., Int. Ed.*, 2021, **60**, 17388–17393.
- 78 H. G. T. Nguyen, M. H. Weston, O. K. Farha, J. T. Hupp and S. T. Nguyen, *CrystEngComm*, 2012, **14**, 4115–4118.
- 79 H. Noh, Y. X. Cui, A. W. Peters, D. R. Pahls, M. A. Ortuno, N. A. Vermeulen, C. J. Cramer, L. Gagliardi, J. T. Hupp and O. K. Farha, *J. Am. Chem. Soc.*, 2016, **138**, 14720–14726.
- 80 P. F. Ji, Y. Song, T. Drake, S. S. Veroneau, Z. K. Lin, X. D. Pan and W. B. Lin, *J. Am. Chem. Soc.*, 2018, **140**, 433–440.
- 81 G. Wang, C. T. He, R. Huang, J. J. Mao, D. S. Wang and Y. D. Li, *J. Am. Chem. Soc.*, 2020, **142**, 19339–19345.
- 82 M. B. Chambers, X. Wang, N. Elgrishi, C. H. Hendon, A. Walsh, J. Bonnefoy, J. Canivet, E. A. Quadrelli, D. Farrusseng, C. Mellot-Draznieks and M. Fontecave, *ChemSusChem*, 2015, **8**, 603–608.
- 83 N. C. Thacker, Z. K. Lin, T. Zhang, J. C. Gilhula, C. W. Abney and W. B. Lin, *J. Am. Chem. Soc.*, 2016, **138**, 3501–3509.
- 84 S. Chen, W. H. Li, W. Jiang, J. Yang, J. Zhu, L. Wang, H. Oh, Z. Zhang, M. Chen, X. Sun, D. S. Wang and Y. D. Li, *Angew. Chem., Int. Ed.*, 2021, DOI: 10.1002/anie.202114450.
- 85 J. H. Li, Z. W. Yu, Z. Gao, J. Q. Li, Y. Tao, Y. X. Xiao, W. H. Yin, Y. L. Fan, C. Jiang, L. J. Sun and F. Luo, *Inorg. Chem.*, 2019, **58**, 10829–10836.
- 86 K. Guo, X. L. Zhu, L. L. Peng, Y. H. Fu, R. Ma, X. Q. Lu, F. M. Zhang, W. D. Zhu and M. H. Fan, *Chem. Eng. J.*, 2021, **405**, 127011.
- 87 G. J. Chen, X. B. Li, C. C. Zhao, H. C. Ma, J. L. Kan, Y. B. Xin, C. X. Chen and Y. B. Dong, *Inorg. Chem.*, 2018, **57**, 2678–2685.
- 88 X. G. Li, C. L. Zhang, M. H. Luo, Q. L. Yao and Z. H. Lu, *Inorg. Chem. Front.*, 2020, **7**, 1298–1306.
- 89 C. Zhang, M. Cui, J. J. Ren, Y. F. Xing, N. Li, H. Y. Zhao, P. Liu, X. P. Ji and M. Li, *Chem. Eng. J.*, 2020, **401**, 126025.
- 90 E. Park, J. Jack, Y. M. Hu, S. Wan, S. F. Huang, Y. H. Jin, P. C. Maness, S. Yazdi, Z. Y. Ren and W. Zhang, *Nanoscale*, 2020, **12**, 2596–2602.
- 91 R. Kamai, K. Kamiya, K. Hashimoto and S. Nakanishi, *Angew. Chem., Int. Ed.*, 2016, **55**, 13184–13188.
- 92 F. P. Lu, Y. Q. Li, Q. R. Shi, C. F. Zhao, S. H. Li and S. P. Pang, *New J. Chem.*, 2020, **44**, 15354–15361.
- 93 Q. P. Zhang, Y. L. Sun, G. Cheng, Z. Wang, H. Ma, S. Y. Ding, B. Tan, J. H. Bu and C. Zhang, *Chem. Eng. J.*, 2020, **391**, 123471.
- 94 Y. Deng, Z. Zhang, P. Y. Du, X. M. Ning, Y. Wang, D. X. Zhang, J. Liu, S. T. Zhang and X. Q. Lu, *Angew. Chem., Int. Ed.*, 2020, **59**, 6082–6089.
- 95 S. L. Lu, Y. M. Hu, S. Wan, R. McCaffrey, Y. H. Jin, H. W. Gu and W. Zhang, *J. Am. Chem. Soc.*, 2017, **139**, 17082–17088.
- 96 P. Pachfule, M. K. Panda, S. Kandambeth, S. M. Shivaprasad, D. D. Diaz and R. Banerjee, *J. Mater. Chem. A*, 2014, **2**, 7944–7952.
- 97 J. C. Wang, C. X. Liu, X. Kan, X. W. Wu, J. L. Kan and Y. B. Dong, *Green Chem.*, 2020, **22**, 1150–1155.
- 98 J. Li, L. H. Zhang, X. T. Liu, N. Z. Shang, S. T. Gao, C. Feng, C. Wang and Z. Wang, *New J. Chem.*, 2018, **42**, 9684–9689.
- 99 P. Pachfule, S. Kandambeth, D. D. Diaz and R. Banerjee, *Chem. Commun.*, 2014, **50**, 3169–3172.
- 100 M. Y. Liu, X. Q. Wang, J. Liu, K. W. Wang, S. B. Jin and B. Tan, *ACS Appl. Mater. Interfaces*, 2020, **12**, 12774–12782.
- 101 M. Y. Fan, W. D. Wang, X. Y. Wang, Y. Y. Zhu and Z. P. Dong, *Ind. Eng. Chem. Res.*, 2020, **59**, 12677–12685.
- 102 Q. Z. Sun, C. Y. Wu, Q. Y. Pan, B. J. Zhang, Y. M. Liu, X. Y. Lu, J. Sun, L. S. Sun and Y. J. Zhao, *ChemNanoMat*, 2021, **7**, 95–99.



- 103 C. Y. Xu, J. Y. Lin, D. Yan, Z. Y. Guo, D. J. Austin, H. B. Zhan, A. Kent and Y. F. Yue, *ACS Appl. Nano Mater.*, 2020, **3**, 6416–6422.
- 104 R. Tao, X. R. Shen, Y. M. Hu, K. Kang, Y. Q. Zheng, S. C. Luo, S. Y. Yang, W. L. Li, S. L. Lu, Y. H. Jin, L. Qiu and W. Zhang, *Small*, 2020, **16**, 1906005.
- 105 L. Y. Li, H. X. Zhao, J. Y. Wang and R. H. Wang, *ACS Nano*, 2014, **8**, 5352–5364.
- 106 L. Y. Li, C. S. Zhou, H. X. Zhao and R. H. Wang, *Nano Res.*, 2015, **8**, 709–721.
- 107 L. Y. Li, H. X. Zhao and R. H. Wang, *ACS Catal.*, 2015, **5**, 948–955.
- 108 P. Bhanja, X. Liu and A. Modak, *ChemistrySelect*, 2017, **2**, 7535–7543.
- 109 Z. F. Wang, C. B. Liu, Y. Huang, Y. C. Hu and B. Zhang, *Chem. Commun.*, 2016, **52**, 2960–2963.
- 110 D. Xu, F. S. Wang, G. Q. Yu, H. Zhao, J. Yang, M. Yuan, X. Y. Zhang and Z. P. Dong, *ChemCatChem*, 2018, **10**, 4569–4577.
- 111 X. Y. Yang, Y. J. He, L. Y. Li, J. N. Shen, J. H. Huang, L. Y. Li, Z. Y. Zhuang, J. H. Bi and Y. Yu, *Chem.–Eur. J.*, 2020, **26**, 1864–1870.
- 112 R. A. Molla, P. Bhanja, K. Ghosh, S. S. Islam, A. Bhaumik and S. M. Islam, *ChemCatChem*, 2017, **9**, 1939–1946.
- 113 H. X. Fu, Z. H. Zhang, W. H. Fan, S. F. Wang, Y. Liu and M. H. Huang, *J. Mater. Chem. A*, 2019, **7**, 15048–15053.
- 114 W. Zhang, Y. Mei, X. Huang, P. Wu, H. H. Wu and M. Y. He, *ACS Appl. Mater. Interfaces*, 2019, **11**, 44241–44248.
- 115 M. Nihei, H. Ida, T. Nibe, A. M. P. Moeljadi, Q. T. Trinh, H. Hirao, M. Ishizaki, M. Kurihara, T. Shiga and H. Oshio, *J. Am. Chem. Soc.*, 2018, **140**, 17753–17759.
- 116 X. X. Gou, T. Liu, Y. Y. Wang and Y. F. Han, *Angew. Chem., Int. Ed.*, 2020, **59**, 16683–16689.
- 117 Z. Z. Wang, C. B. Reddy, X. Zhou, J. J. Ibrahim and Y. Yang, *ACS Appl. Mater. Interfaces*, 2020, **12**, 53141–53149.
- 118 N. N. Sun, C. M. Wang, H. L. Wang, L. Yang, P. Jin, W. Zhang and J. Z. Jiang, *Angew. Chem., Int. Ed.*, 2019, **58**, 18011–18016.
- 119 B. Mondal and P. S. Mukherjee, *J. Am. Chem. Soc.*, 2018, **140**, 12592–12601.
- 120 F. R. Fortea-Perez, M. Mon, J. Ferrando-Soria, M. Boronat, A. Leyva-Perez, A. Corma, J. M. Herrera, D. Osadchii, J. Gascon, D. Armentano and E. Pardo, *Nat. Mater.*, 2017, **16**, 760.
- 121 G. Huang, L. Yang, Q. Yin, Z. B. Fang, X. J. Hu, A. A. Zhang, J. Jiang, T. F. Liu and R. Cao, *Angew. Chem., Int. Ed.*, 2020, **59**, 4385–4390.
- 122 H. B. Fang, J. X. Chen, Y. L. Xiao and J. Y. Zhang, *Appl. Catal., A*, 2019, **585**, 117186.
- 123 M. A. Ziaee, H. Zhong, C. Y. Cui and R. H. Wang, *ACS Sustainable Chem. Eng.*, 2018, **6**, 10421–10428.
- 124 Y. Q. Su, X. J. Li, Y. X. Wang, H. Zhong and R. H. Wang, *Dalton Trans.*, 2016, **45**, 16896–16903.
- 125 H. B. Fang, S. J. Sun, P. S. Liao, Y. Hu and J. Y. Zhang, *J. Mater. Chem. A*, 2018, **6**, 2115–2121.
- 126 H. X. Zhao, Y. X. Wang and R. H. Wang, *Chem. Commun.*, 2014, **50**, 10871–10874.
- 127 P. F. Zhang, Z. A. Qiao, X. G. Jiang, G. M. Veith and S. Dai, *Nano Lett.*, 2015, **15**, 823–828.
- 128 S. Y. Zhang, Z. Kochovski, H. C. Lee, Y. Lu, H. M. Zhang, J. Zhang, J. K. Sun and J. Y. Yuan, *Chem. Sci.*, 2019, **10**, 1450–1456.
- 129 Y. J. Chen, R. Gao, S. F. Ji, H. J. Li, K. Tang, P. Jiang, H. B. Hu, Z. D. Zhang, H. G. Hao, Q. Y. Qu, X. Liang, W. X. Chen, J. C. Dong, D. S. Wang and Y. D. Li, *Angew. Chem., Int. Ed.*, 2021, **60**, 3212–3221.
- 130 J. W. Wan, Z. H. Zhao, H. S. Shang, B. Peng, W. X. Chen, J. J. Pei, L. R. Zheng, J. C. Dong, R. Cao, R. Sarangi, Z. L. Jiang, D. N. Zhou, Z. B. Zhuang, J. T. Zhang, D. S. Wang and Y. D. Li, *J. Am. Chem. Soc.*, 2020, **142**, 8431–8439.
- 131 Q. Y. Qu, S. F. Ji, Y. J. Chen, D. S. Wang and Y. D. Li, *Chem. Sci.*, 2021, **12**, 4201–4215.
- 132 X. L. Hu, G. Luo, Q. N. Zhao, D. Wu, T. X. Yang, J. Wen, R. H. Wang, C. H. Xu and N. Hu, *J. Am. Chem. Soc.*, 2020, **142**, 16776–16786.
- 133 D. Zhou, J. G. Yi, X. D. Zhao, J. Q. Yang, H. R. Lu and L. Z. Fan, *Chem. Eng. J.*, 2021, **413**, 127508.
- 134 Z. K. Kou, W. J. Zang, Y. Y. Ma, Z. H. Pan, S. C. Mu, X. R. Gao, B. S. Tang, M. Xiong, X. J. Zhao, A. K. Cheetham, L. R. Zheng and J. Wang, *Nano Energy*, 2020, **67**, 104288.
- 135 H. B. Wu, B. Y. Xia, L. Yu, X. Y. Yu and X. W. Lou, *Nat. Commun.*, 2015, **6**, 6512.
- 136 Y. J. Chen, S. F. Ji, Y. G. Wang, J. C. Dong, W. X. Chen, Z. Li, R. A. Shen, L. R. Zheng, Z. B. Zhuang, D. S. Wang and Y. D. Li, *Angew. Chem., Int. Ed.*, 2017, **56**, 6937–6941.
- 137 Y. Wang, J. L. Li, W. X. Shi, Z. M. Zhang, S. Guo, R. Si, M. Liu, H. C. Zhou, S. Yao, C. H. An and T. B. Lu, *Adv. Energy Mater.*, 2020, **10**, 2002138.
- 138 T. H. Gu, W. Teng, N. Bai, Z. H. Chen, J. W. Fan, W. X. Zhang and D. Y. Zhao, *J. Mater. Chem. A*, 2020, **8**, 9545–9553.
- 139 Z. Li, Y. J. Chen, S. F. Ji, Y. Tang, W. X. Chen, A. Li, J. Zhao, Y. Xiong, Y. E. Wu, Y. Gong, T. Yao, W. Liu, L. R. Zheng, J. C. Dong, Y. Wang, Z. B. Zhuang, W. Xing, C. T. He, C. Peng, W. C. Cheong, Q. H. Li, M. L. Zhang, Z. Chen, N. H. Fu, X. Gao, W. Zhu, J. W. Wan, J. Zhang, L. Gu, S. Q. Wei, P. J. Hu, J. Luo, J. Li, C. Chen, Q. Peng, X. F. Duan, Y. Huang, X. M. Chen, D. S. Wang and Y. D. Li, *Nat. Chem.*, 2020, **12**, 764–772.
- 140 S. F. Ji, Y. J. Chen, Q. Fu, Y. F. Chen, J. C. Dong, W. X. Chen, Z. Li, Y. Wang, L. Gu, W. He, C. Chen, Q. Peng, Y. Huang, X. F. Duan, D. S. Wang, C. Draxl and Y. D. Li, *J. Am. Chem. Soc.*, 2017, **139**, 9795–9798.
- 141 M. R. Zhang, V. Singh, X. F. Hu, X. Y. Ma, J. K. Lu, C. Zhang, J. P. Wang and J. Y. Niu, *ACS Catal.*, 2019, **9**, 7641–7650.
- 142 Y. T. Xu, X. F. Xiao, Z. M. Ye, S. L. Zhao, R. G. Shen, C. T. He, J. P. Zhang, Y. D. Li and X. M. Chen, *J. Am. Chem. Soc.*, 2017, **139**, 5285–5288.
- 143 D. Chakraborty, S. Nandi, R. Illathvalappil, D. Mullangi, R. Maity, S. K. Singh, S. Haldar, C. P. Vinod, S. Kurungot and R. Vaidhyanathan, *ACS Omega*, 2019, **4**, 13465–13473.



- 144 A. J. Han, W. X. Chen, S. L. Zhang, M. L. Zhang, Y. H. Han, J. Zhang, S. F. Ji, L. R. Zheng, Y. Wang, L. Gu, C. Chen, Q. Peng, D. S. Wang and Y. D. Li, *Adv. Mater.*, 2018, **30**, 1706508.
- 145 M. L. Wang, Y. Zhang, M. Z. Cui, Y. Lu, D. D. Peng, X. Cao, C. Wu, J. D. Zhou, Y. Feng, W. F. Liu, Z. F. Chen, X. G. Liu, T. Wang, P. Song and Y. Z. Huang, *Biosens. Bioelectron.*, 2020, **165**, 112373.
- 146 J. H. Zhang, W. Yang, M. Zhang, H. J. Wang, R. Si, D. C. Zhong and T. B. Lu, *Nano Energy*, 2021, **80**, 105542.
- 147 K. X. Huang, J. H. Hua, G. G. Chang, Z. H. Li, G. Tian, M. J. Chen, J. X. Li, S. C. Ke, X. Y. Yang and B. L. Chen, *Small*, 2021, **17**, 2002811.
- 148 T. He, S. M. Chen, B. Ni, Y. Gong, Z. Wu, L. Song, L. Gu, W. P. Hu and X. Wang, *Angew. Chem., Int. Ed.*, 2018, **57**, 3493–3498.
- 149 X. Wang, W. X. Chen, L. Zhang, T. Yao, W. Liu, Y. Lin, H. X. Ju, J. C. Dong, L. R. Zheng, W. S. Yan, X. S. Zheng, Z. J. Li, X. Q. Wang, J. Yang, D. S. He, Y. Wang, Z. X. Deng, Y. E. Wu and Y. D. Li, *J. Am. Chem. Soc.*, 2017, **139**, 9419–9422.
- 150 X. F. Lu, L. Yu, J. T. Zhang and X. W. Lou, *Adv. Mater.*, 2019, **31**, 1900699.
- 151 Q. H. Li, W. X. Chen, H. Xiao, Y. Gong, Z. Li, L. R. Zheng, X. S. Zheng, W. S. Yan, W. C. Cheong, R. A. Shen, N. H. Fu, L. Gu, Z. B. Zhuang, C. Chen, D. S. Wang, Q. Peng, J. Li and Y. D. Li, *Adv. Mater.*, 2018, **30**, 1800588.
- 152 J. Zhao, R. X. Qin and R. Liu, *Appl. Catal., B*, 2019, **256**, 117778.
- 153 C. Wu, Z. F. Chen, M. M. Wang, X. Cao, Y. Zhang, P. Song, T. Y. Zhang, X. L. Ye, Y. Yang, W. H. Gu, J. D. Zhou and Y. Z. Huang, *Small*, 2020, **16**, 2001686.
- 154 Z. F. Liang, D. W. Yang, P. Y. Tang, C. Q. Zhang, J. J. Biendicho, Y. Zhang, J. Llorca, X. Wang, J. S. Li, M. Heggen, J. David, R. E. Dunin-Borkowski, Y. T. Zhou, J. R. Morante, A. Cabot and J. Arbiol, *Adv. Energy Mater.*, 2021, **11**, 2003507.
- 155 P. Pachfule, X. C. Yang, Q. L. Zhu, N. Tsumori, T. Uchida and Q. Xu, *J. Mater. Chem. A*, 2017, **5**, 4835–4841.
- 156 J. Romero, D. Rodriguez-San-Miguel, A. Ribera, R. Mas-Balleste, T. F. Otero, I. Manet, F. Liscio, G. Abellan, F. Zamora and E. Coronado, *J. Mater. Chem. A*, 2017, **5**, 4343–4351.
- 157 J. T. Ren, L. Chen, D. D. Yang and Z. Y. Yuan, *Appl. Catal., B*, 2020, **263**, 118352.
- 158 Z. P. Shi, K. Q. Nie, Z. J. Shao, B. X. Gao, H. L. Lin, H. B. Zhang, B. L. Liu, Y. X. Wang, Y. H. Zhang, X. H. Sun, X. M. Cao, P. Hu, Q. S. Gao and Y. Tang, *Energy Environ. Sci.*, 2017, **10**, 1262–1271.
- 159 J. S. Li, Y. Wang, C. H. Liu, S. L. Li, Y. G. Wang, L. Z. Dong, Z. H. Dai, Y. F. Li and Y. Q. Lan, *Nat. Commun.*, 2016, **7**, 11204.
- 160 X. Q. Wang, Z. Chen, X. Y. Zhao, T. Yao, W. X. Chen, R. You, C. M. Zhao, G. Wu, J. Wang, W. X. Huang, J. L. Yang, X. Hong, S. Q. Wei, Y. Wu and Y. D. Li, *Angew. Chem., Int. Ed.*, 2018, **57**, 1944–1948.
- 161 L. Jiao, G. Wan, R. Zhang, H. Zhou, S. H. Yu and H. L. Jiang, *Angew. Chem., Int. Ed.*, 2018, **57**, 8525–8529.
- 162 W. X. Cao, L. Lin, H. F. Qi, Q. He, Z. J. Wu, A. Q. Wang, W. H. Luo and T. Zhang, *J. Catal.*, 2019, **373**, 161–172.
- 163 F. T. Kong, X. H. Fan, X. Y. Zhang, L. Y. Wang, A. G. Kong and Y. K. Shan, *Carbon*, 2019, **149**, 471–482.
- 164 Q. Zuo, P. P. Zhao, W. Luo and G. Z. Cheng, *Nanoscale*, 2016, **8**, 14271–14277.
- 165 L. Y. Chen, L. Zhang, Z. J. Chen, H. J. Liu, R. Luque and Y. W. Li, *Chem. Sci.*, 2016, **7**, 6015–6020.
- 166 S. J. Wei, Y. Wang, W. X. Chen, Z. Li, W. C. Cheong, Q. H. Zhang, Y. Gong, L. Gu, C. Chen, D. S. Wang, Q. Peng and Y. D. Li, *Chem. Sci.*, 2020, **11**, 786–790.
- 167 X. Wei, D. Zheng, M. Zhao, H. Z. Chen, X. Fan, B. Gao, L. Gu, Y. Guo, J. B. Qin, J. Wei, Y. L. Zhao and G. C. Zhang, *Angew. Chem., Int. Ed.*, 2020, **59**, 14639–14646.
- 168 J. Mahmood, F. Li, S. M. Jung, M. S. Okyay, I. Ahmad, S. J. Kim, N. Park, H. Y. Jeong and J. B. Baek, *Nat. Nanotechnol.*, 2017, **12**, 441–446.

